ARUN POUDEL

PREPARATION OF Yb^{3+} AND Er^{3+} CODOPED PHOSPHATE GLASSES FOR ACTIVE WAVEGUIDES

Master of Science Thesis

ABSTRACT

ARUN POUDEL: Preparation of Yb^{3+} and Er^{3+} codoped phosphate glasses for active waveguides

Fibers and fiber lasers are widely used in photonics as well as in medical applications. Hence, research on fiber lasers utilizing glasses activated with rare-earth (RE) ions has been of great interest. One of the most studied fiber laser glass is Erbium-doped silicate glasses. However, low solubility of Er^{3+} ions in silicate glasses results in Er−Er cluster formation for higher concentrations. Phosphate glasses are able to accommodate a larger amount of rare earth dopants compared to silicate glasses because of their two dimensional structure, which makes these glasses prospective candidates for different applications ranging from telecommunication systems, upconverters, fibers, optical amplifiers and solid-state lasers.

In this thesis, we explored the possibility of using RE-doped phosphate-based glasses for planar waveguides and fiber lasers. Er^{3+} and Yb^{3+} codoped phosphate glasses were prepared using melt quenching method with different concentration of ZnO and Y_2O_3 and these glasses were optimized for thin film deposition and fiber drawing. From the thermal properties of the glasses, all the investigated glasses are expected to have a good thermal stability against crystallization which is a crucial property when depositing the glass into films and also when drawing it into fiber. The changes in the structural properties induced by the changes in the glass composition were studied with infrared and Raman spectroscopies. Based on the optical and luminescence properties of the glasses, the RE sites are not expected to be strongly affected by the change in the glass composition.

The glass with composition ($49P_2O_5$-$39.2SrO$-$9.8Na_2O$-$0.5Er_2O_3$-$1.5Yb_2O_3$) (in mol%) was selected for film deposition and preform casting. Thin film was deposited using e-beam evaporation. However, films contained no heavier RE atoms and they suffered serious spallation and delamination upon aging. Nevertheless, single core fiber with a 115 μm diameter was successfully drawn from a 10 cm long preform with 1 cm diameter. Losses were estimated using cutback method and found to be 0.1–0.4 dB·cm^{-1} at 700 nm. Emission spectra from fiber showed a broadband centered at 1.5 μm and the bandwidth measured greater than 70 nm. The broad luminescence source is highly demanded in several applications such as LIDAR or optical coherence tomography. The spectral hole-burning effect was observed in the phosphate fiber with the length exceeding 3 cm which could be interesting for ultra-high density optical data storage.

PREFACE

The research work presented in this thesis was carried out in Photonic Glasses Group at Laboratory of Photonics, Tampere University of Technology. I am deeply grateful to the administration for giving me the opportunity to work in an excellent research environment.

I would like to offer special thanks to my thesis advisors, Assistant Professor Laeticia Petit and Associate Professor Tapio Niemi, whose scientific acumen and positive encouragement have guided my research. I extend my gratitude and eternal thanks for your endless patience and support. There would be no thesis without your insightful guidance and experience.

I am indebted to Regima Gumenyuk for her help in the laboratory in characterizing the fiber and for her helpful discussions, Turkka Salminen for SEM and Raman spectroscopy and Amy Nommeots-Nomm for thermal analysis of my samples. I am particularly grateful for the assistance given by Jarno Reuna and Jari Nikkinen on e-beam evaporator operation and thin-film deposition. I thank our French partners from Rennes University (France) for fiber drawing.

I dedicate this thesis to my father Lila Prasad Poudel and mother Manrupa Poudel for their unconditional love and affection. I would like to show my due respect to my family for their care and support.

Finally, to my beloved wife Dristi, thank you for your support and encouragement.

Tampere, 08.08.2017

Arun Poudel

CONTENTS

LIST OF FIGURES

LIST OF SYMBOLS AND ABBREVIATIONS

2D	Two-dimensional
3D	Three-dimensional
BC	Before birth of Christ
CVD	Chemical vapor deposition
CTE	Coefficient of thermal expansion
e-beam	Electron beam
EDS	Energy Dispersive Spectroscopy
NIR	Near infrared
NA	Numerical aperture
PVD	Physical vapor deposition
SEM	Scanning Electron Microscopy
UV	Ultraviolet
VIS	Visible
XRD	X-ray diffraction
TIR	Total internal reflection

λ	*Wavelength*
μm	*Micrometer*
n	*Refractive index*
nm	*Nanometer*
mW	*Milliwatt*
T_g	*Glass transition temperature*
T_x	*Crystallization temperature*
T_p	*Crystallization peak temperature*
T_f	*Fictive temperature*
Θ_a	*Angle of acceptance*
Θ_c	*Critical angle*
Θ_i	*Incident angle*
Θ_r	*Refracted angle*
λ_{ex}	*Excitation wavelength*

1. INTRODUCTION

The first Er^{3+} doped silica glass laser was demonstrated by Snitzer and Woodcock in 1965 with emission at 1.5 μm given by the $^4I_{13/2} \rightarrow ^4I_{15/2}$ transition [Sn 1965]. Even though Er^{3+} is a three level system, room temperature operation was possible due to codoping with Yb^{3+} used as a sensitizer ion that has a strong absorption at ~975 nm. Because of energy resonance between $^2F_{5/2}$ in Yb^{3+} and $^4I_{11/2}$ in Er^{3+}, the energy from Yb^{3+} is transferred to the Er^{3+} ions by energy transfer mechanism. Silica glass has a 3D network made of silica tetrahedral units. Therefore, this compact network cannot incorporate high concentration of RE dopants. Using phosphate glasses as glass host, the properties of $Yb^{3+}-Er^{3+}$ glass laser has been improved a lot [Mi 2001].

Phosphate glasses possess very important features like good thermal and mechanical stabilities, high UV transparency, low dispersion and low melting temperature [Sc 2004]. In addition, the two dimensional (2D) structure of the phosphate network accepts a wide range of RE metal ions that makes phosphate glasses good candidates for lasers and amplifier media [Kr 1979].

Phosphate glasses have been intensively researched with different modifiers and network formers in order to enhance the gain bandwiths of optical amplifiers. As reported in [Li 1997], same metal oxide in phosphate glass could play dual role as a network modifier or as a network former depending upon the glass composition. Thus, changing only the composition of glass, RE sites and be varied to get better performance in phosphate glass.

Glasses can be prepared using various techniques; in chemical vapor deposition (CVD) glass forming oxides in gaseous form are reacted to obtain amorphous film and the subsequent deposition for longer time will result in bulk glass [Ma 2009]. Sol gel technique involves hydrolysis and condensation of metal alkoxide precursor. Using solgel dense film, bulk glass, glass nanoparticles can easily be prepared [Ri 2004]. However, the most simple and widely used glass processing technique is melt-quenching method in which molten glass compound is cooled down suddenly to a rigid condition without allowig time for the nucleation and crystal growth. This method allows flexibility to melt innumerable compositions of the glasses at a same time. This easy and handy method was used to prepare the investigated glasses in this work.

The main objective of this thesis is to fabricate planar (thin film) and fiber active waveguides from active phosphate glasses prepared by standard melting process. Here, new phosphate glasses within the system $(98-x-y)(0.50P_2O_5-0.40SrO-0.10Na_2O)-0.5Er_2O_3-1.5Yb_2O_3-xZnO-yY_2O_3$ (in mol%) were prepared and characterized in order to

find a new glass which could be deposited into thin films and/or drawn into fibers. To be considered as a good candidate for film deposition and fiber drawing, this glass should have a good thermo-mechanical resistance and thermal stability against crystallization and should exhibit also high absorption and emission properties.

Chapter 2 gives the theoritical background of this thesis. It starts with the definition and history of glass. Basic terms like glass transition temperature (T_g) and crystallization temperature (T_x) are introduced, which are the main factors to determine the thermal stability of glass. The difference between the stucture of phosphate and commercial silica glasses is discussed. $Yb^{3+}-Er^{3+}$ codoped laser glasses is presented. Structure, working principle and fabrication methods of planar and fiber waveguides is briefly described in the last part of the chapter.

Chapter 3 includes the description of the glass preparation, film deposition and fiber drawing. It also includes the description of the equipment used for the materials characterization.

Chapter 4 includes the main findings. First, the glass selection procedure is discussed followed by our findings on thin film deposition and fiber drawing.

Finally, conclusion of this thesis is presented in chapter 5.

2. BACKGROUND

2.1 Definition and History of Glass

According to Zachariasen [Za 1932], '*a silica glass has an extended three-dimensional network and its energy content is comparable to that of the corresponding crystal but without periodicity and symmetry.*' This definition explores the principle difference between a crystal network and a glass network. However, scientists have defined glass according to their field of expertise in many different ways [Kr 2016]. Here, a glass can be defined as *an inorganic product of fusion, which has been cooled to a rigid condition without crystallization.* This definition reflects the standard melt quenching process of glass making where a batch of finely crushed raw materials is melted in a high temperature furnace and the liquid is cooled down suddenly to get amorphous glass.

Production of glass has a long history that date back to 2500 BC when the first glass object was found in Syria. Later in 2450 BC glass beads were plentiful in Mesopotamia. Rasmussen in his book 'How glass changed the world' hypothesized that the glass was discovered either as a byproduct of metallurgy or from an evolutionary sequence in the development of ceramic materials [Ra 2012]. In metallurgy process, a glassy solid similar to obsidian, a naturally occurring silica-based material, was obtained when slag was cooled. The other possible discovery might be the accidental variation in some parameters like poor composition or temperature control in production of faience, which was an ancient material containing mainly silica along with small amounts of soda and other impurities. Nevertheless, glass is now used extensively, in solar cells, windmill turbine blades, water purifiers, nuclear waste management, hydrogen storage, etc. [Br 2009].

2.2 Glass formation

Materials that exhibit glass transition behavior can be taken as glass. Either liquid can crystallize below the melting temperature (T_m) or the melt can be cooled down below melting temperature without crystallization to form supercooled liquid. When a liquid is allowed to cool very slowly to the temperature below the melting temperature, it changes to crystal if the kinetics favors the nucleation of crystalline phase [Fa 2003]. The volume decreases abruptly at this point. The nucleation and crystal growth rate depend, both, on the viscosity of the supercooled liquid and also on the difference in free energy between crystal and glass, ΔG_v [Ya 2000]. Nevertheless, if the liquid is cooled while avoiding the nucleation of crystal, it transforms to supercooled liquid. As temperature is further decreased, the structure of glass continues to rearrange without sudden change in volume or enthalpy because of discontinuous structural rearrangement of the molecules.

The glass formation of any liquid can be understood looking at the volume or enthalpy vs temperature curve (**Figure 1**).
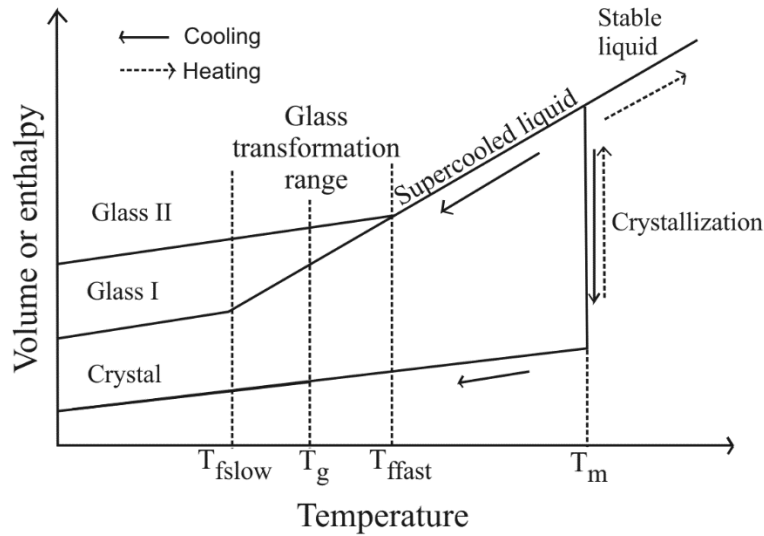
Figure 1. *Schematic plot of glass formation [Fa 2003]*

As seen in **Figure 1**, the fast and slow cooling rates lead to the formation of glasses with different volumes. The extrapolation of supercooled line and glass lines intersects at a point, which is defined as fictive temperature (T_f). T_{fslow} and T_{ffast} are fictive temperatures for slow cooling and fast cooling rate, respectively. Thus, the fictive temperature depends on the thermal history and it is an important parameter to define as it has a significant effect on the various properties of the glass. The glass transition temperature (T_g) is defined in between T_{fslow} and T_{ffast} to denote the onset of glass transformation.

As illustrated in **Figure 2a** taken SiO_2 as an example, crystals have distinct internal structures, which result in a distinctive pattern in X-ray diffractogram that can be used to identify the specific material.
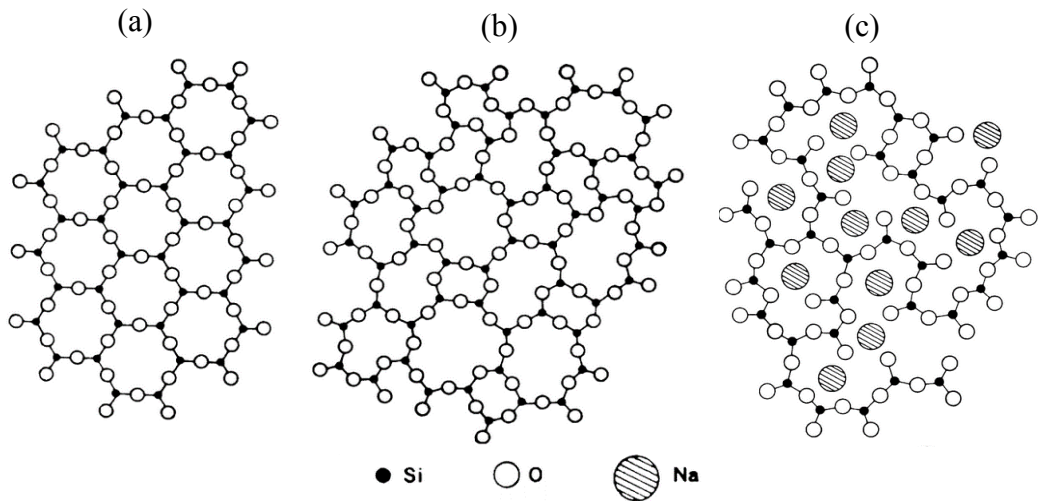
Figure 2. *Molecular structure: crystal of silicon dioxide (a) and Amorphous silicon dioxide (glass) (b) and glass with a network modifier (c) [Ya 2000]*

However, glasses have only short-range structure made of interconnected structural blocks but without regular long-range arrangements (**Figure 2b**). Both the coordination number and interatomic distances are uneven in the material. Thus, glass does not give well-resolved x-ray diffraction patterns and does not have well-defined melting point like a crystalline solid. Instead, it tends to soften slowly over a wide temperature range.

Chemist Tom Husband in his article 'The sweet science of candy making' [Hu 2014] explains that even sugar crystals can be turned to glassy candies if it is cooled fast enough allowing no time for the crystal formation. For an instance, in cotton candy, glass threads are formed when filaments of liquid sugar from tiny nozzles of the machine cools immediately in air. The dissolved sucrose molecules bind with one another, but cannot attain any special order so the candy takes appearance of glass and is amorphous in nature.

Many oxides, halides, and chalcogenide systems with appropriate size can form amorphous solids with atomic arrangements. Randomly arranged strong bonds are developed by components called network formers. Nevertheless, these bonds can be modified by various components called network modifiers, which modify the glass properties by occupying thermodynamically stable sites in the structure as shown in **Figure 2c**. This gives glass flexibility of chemical composition and makes easy for doping, as it does not require stoichiometry among constituents unless the electrical neutrality over the whole structure

2.3 Silicate and phosphate glasses

Typically, pure silica glasses have very high glass transition temperature (~1200°C), small thermal expansion coefficient and high melting temperature [Heraeus]. It is possible to produce glasses with modified viscosity and other optical properties, lower melting point, good chemical resistance, etc. by using various oxides as network modifiers. For an instance, most commercial glasses, soda-lime-silica glasses, are basically mixtures of silica (70–74%), sodium oxide (12–16%) and calcium oxide (5–11%). Tetrahedral structure of SiO_2 allows forming glass on its own and provides a base for other mixed-oxide glasses.

Silica glass consists of SiO_4 tetrahedral where oxygen atoms are connected with two silicon atoms forming $Si-O-Si$ bonds as shown in **Figure 3**.
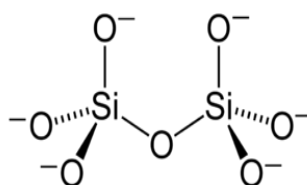
Figure 3. *Tetrahedra structure of SiO₄ forming Si−O−Si bonds*

In SiO_4 tetrahedral, all the oxygens are bridging oxygen and corners are shared in three dimensions. Bridging oxygen atoms link glass forming tetrahedral units while the non-bridging oxygen forms ionic bonds with modifiers. In quartz, SiO_4 tetrahedra units have well defined Si−O (1.62 Å) and O−O (2.65 Å) bond length whereas in silica glass, the Si−O−Si bond angle varies (~144±10°) which is responsible for the short range order. The silica network can be described as a compact rigid 3D network leading to low solubility of the RE ions, resulting in the formation of RE clusters for high RE concentrations.

Phosphorus pentoxide (P_2O_5) is one of the glass forming oxides that has a long history of being researched as a potential candidate for laser application [Kr 1979]. Phosphate glasses possess interesting properties such as low glass transition temperatures (T_g) and high coefficient of thermal expansion, for example [Br 1997]. In addition, phosphate glasses exhibit anomalous compositional dependence of properties such as T_g, density, and refractive index and these anomalies depend on the type of network modifiers [Br 2000].

Phosphate glass structure consists of PO_4 tetrahedral connected through P−O−P linkages forming a polymeric arrangement. The PO_4 tetrahedrons have three long single bond with bridging oxygen atom and one short double bond with terminal oxygen as shown in the **Figure 4.** They are linked together with covalent bonding in chains or rings by a bridging oxygen atoms. Tetrahedral units in phosphate glass are described by the Q^n terminology where n represents the number of bridging oxygen atoms per PO_4 tetrahedron.
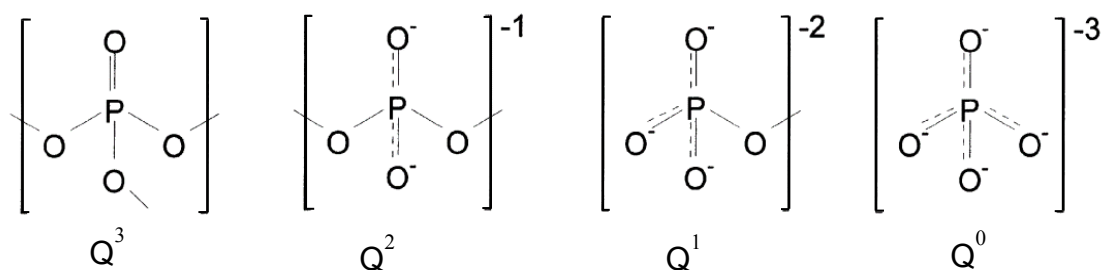
Figure 4. *Network units in phosphate glasses [Br 2000]*

The structure of the vitreous v-P_2O_5 consists of Q^3 P-tetrahedra with three bridging oxygen and one double bonded oxygen P=O, forming a three-dimensional cross-linked network. By adding the modifier oxide, the phosphate structural groups pass from ultraphosphate (Q^3) to polymer like metaphosphate chain (Q^2) to inert glasses based on small pyrophosphate (Q^1) and orthophosphate (Q^0) anions depending on the [O]/[P] ratio as set by the glass composition [Br 2000].

The poor mechanical stability due to their 2D structure. However, durable and strong phosphate glasses can be realised if the these glasses are doped with different metallic

compositions like Sodium, Iron, Zinc, etc. [Ka 2001]. Nevertheless, 2D network of tetrahedral provides phosphate glasses unique and advantageous properties over silica glasses like high concentration of rare-earth ion doping [Kr 1979][Ya 2000].

2.4 Laser glasses

The first solid-state laser (ruby laser- crystalline alumina (Al_2O_3) in which a small fraction of the Al^{3+} ions was replaced by chromium ions, Cr^{3+}) was invented in 1960 and Nd-glass laser in 1961 [Ga 2006]. Since then laser glasses have been the most studied photonic glasses. Laser glasses are doped with laser-active rare earth ions, which are in lanthanide series in periodic table. These ions absorb pump light, typically at a shorter wavelength than the laser or amplifier wavelength (except in upconversion lasers), which excites them into some metastable levels [Pa 2008].

The most important laser glasses for IR region are glasses doped with Pr^{3+}, Nd^{3+}, Tm^{3+}, Er^{3+}, Ho^{3+}, and Yb^{3+} ions. The potential application bands of some RE ions in glass and energy transition are shown in the **Table 1** [Ga 2006].

Table 1. Potential amplification bands of some rare-earth ions in glass

Operating range (nm)	Dopant RE ion	Transition
1050-1150	Yb^{3+}	$^2F_{5/2} \rightarrow \,^2F_{7/2}$
1260-1350	Pr^{3+}	$^1G_4 \rightarrow \,^3H_5$
1320-1400	Nd^{3+}	$^4F_{3/2} \rightarrow \,^4I_{13/2}$
1460-1510	Tm^{3+}	$^3H_4 \rightarrow \,^3F_4$
1500-1600	Er^{3+}	$^4I_{13/2} \rightarrow \,^4I_{15/2}$
1600-1650	Ho^{3+}	$^5I_5 \rightarrow \,^5I_7$
1700-2015	Tm^{3+}	$^3F_4 \rightarrow \,^3F_6$

The most studied rare-earth elements for laser glasses in NIR is erbium. The unique feature of erbium ions including other rare-earth ions is inner 4f shell that is incompletely filled (electronic configuration of erbium: [Kr] $4d^{10}4f^{11}5s^25p^6$, where [Kr] is electronic configuration for krypton).

Different electron-electron interactions and spin-orbit couplings in partially empty 4f shell give rise to a number of discrete energy levels as shown in **Figure 5**.
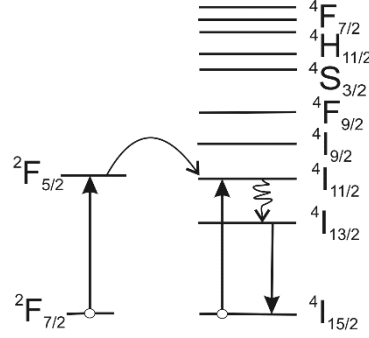
Figure 5. *Energy level diagram of Yb^{3+} and Er^{3+} and emission at 1.5 μm*

The most important laser wavelength in Er^{3+} doped laser glasses is at NIR region (1.5-1.6 μm) which is due to the $^4I_{13/2} \rightarrow {^4I_{15/2}}$ transition. When pumped at 975 nm, Er^{3+} ions are excited to the $^4I_{11/2}$ level. Due to very short lifetime in this excited state, the Er^{3+} ions decay to the $^4I_{13/2}$ with non-radiative transition. This causes population inversion at $^4I_{13/2}$ and also emission at 1.5 μm due to the $^4I_{13/2} \rightarrow {^4I_{15/2}}$ transition. However, Er^{3+} ions have very weak absorption at 980 nm. In order to increase the absorption at 980 nm, Yb^{3+} can be used as a co-dopant. Yb^{3+} ions have simple energy scheme which overlaps with the weak absorption band in Er^{3+} ions as shown in **Figure 5**. In addition, Yb^{3+} ions have a large absorption cross-section at 975 nm. Thus, most of the Er^{3+} laser glasses are codoped with Yb^{3+} to increase the pump rate at 975 nm by efficient energy transfer from Yb^{3+} to Er^{3+}. The Yb$^{3+} \rightarrow$ Er^{3+} energy transfer rate depends on the host material.

2.5 Waveguides

A waveguide is an optical structure that allows the confinement of light within its boundaries by total internal reflection (TIR) [Li 2003]. TIR is reflecting light back in the same medium when it passes from high refractive index (n_1) medium to low refractive index (n_2) medium. The mechanism of TIR is shown in the **Figure 6**.
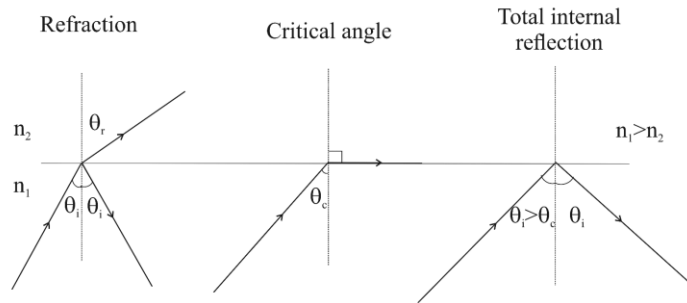
Figure 6. *Ray optics for total internal reflection*

An incident angle (θ_i) for which the refracted angle (θ_r) takes the value of $\pi/2$ radians is called the critical angle θ_c, which is given by equation (1).

$$\theta_c = sin^{-1}(n_2 / n_1) \tag{1}$$

When $\theta_i < \theta_c$, partial reflection and refraction occurs at the interface but when θ_i exceeds θ_c, the incident light is totally reflected.

Waveguides can be realized in various geometries as illustrated in **Figure 7**.

(a)   (b)   (c)
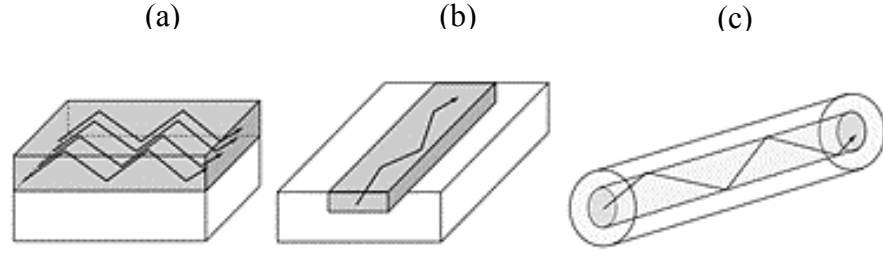
Figure 7. *Schematic diagram of planar waveguide (a and b) and fiber waveguide (c)*

In general, the structure of a waveguide consists of 2 different materials with different refractive indices so the light is confined in the material with the higher refractive index. In the **Figure 7**, darker region represent higher index material and light propagation due to TIR is shown by ray diagram within.

Rays coming to the waveguide at larger angle cannot attain total internal reflection at the interface and thus there exists a maximum angle for which input light rays will be guided through the waveguide. This is referred as a numerical aperture (NA) of the waveguide and is related to the critical angle θ_c as show in **Figure 8**.
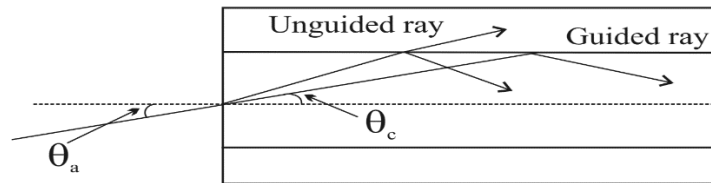
Figure 8. *Schematic diagram to illustrate numerical aperture of a waveguide*

Snell's law at the input face of waveguide gives the value of NA as in equation (2).

$$NA = \sin \theta_a = n_1 \sin \theta_c = (n_1^2 - n_2^2)^{1/2} \tag{2}$$

Maximizing NA would make possible to couple light as much as possible and this can be achieved by increasing the difference between the refractive indices.

2.5.1 Planar waveguides

In planar waveguide configuration, light confinement in the guiding layer can be achieved in two major approaches. Either a thin film of high refractive index can be deposited on a substrate of low refractive index. It is also possible to increase locally the refractive index of a bulk material using different techniques such as ion exchange, ion implantation, UV writing of femtosecond laser writing.

Figure 9 presents the different schemes for thin film deposition. Wise selection of thin film deposition technique has to be made depending on the composition of the target material as applied process along with the different deposition parameters and the composition of the target material have a significant impact on the final film quality.
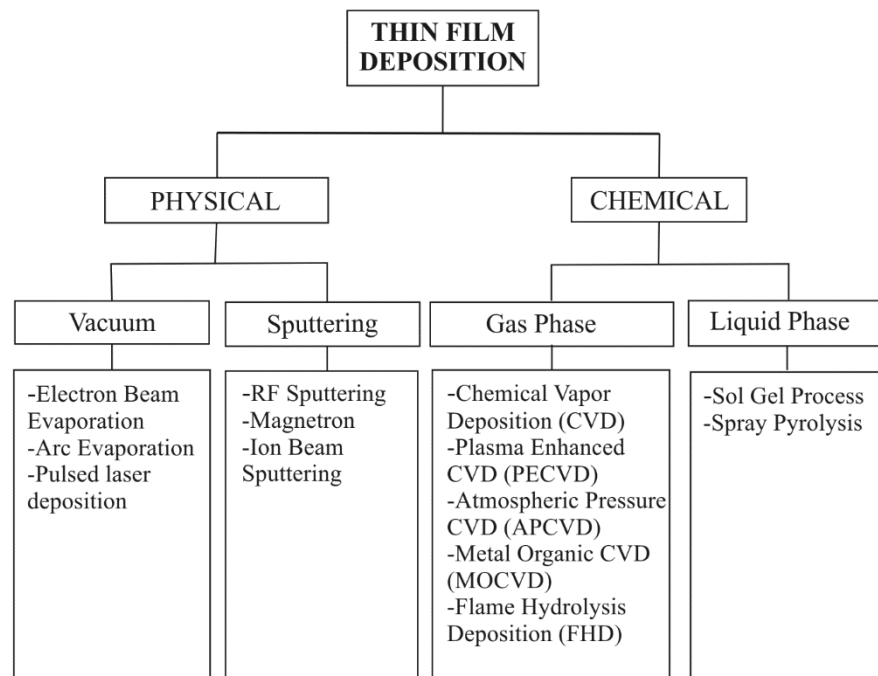
Figure 9. *Fabrication process for glass waveguides [Ri 2004]*

Thin films can be deposited using different techiques such as physical vapor deposition (PVD), electron beam evaporation, sputtering, etc. where the target is heated using an elecron beam or it is bombarded with ions in a low vaccum environment. Chemical processes like chemical vapor deposition (CVD) is also very popular thin-film deposition technique where, two or more precusors are vaporised to react together on a substrate to get film of desired composition. In liquid phase, precursor with desired composition and good viscosity can be either directly spin coated or sprayed over a substrate. After heat treatment, fine film can be obtained. In this thesis the planar waveguides were prepared by e-beam evaporation.

In an e-beam system, the entire process of deposition takes place in a vacuum chamber. Flux of electrons is produced by the electron gun (tungsten filament) and is accelerated to high kinetic energy. The beam is bent and directed towards the crucible using magnets. Upon striking the target, electrons lose energy which is converted to heat melting the surface of the film target. A typical e-beam evaporation chamber is depicted in the **Figure 10**.
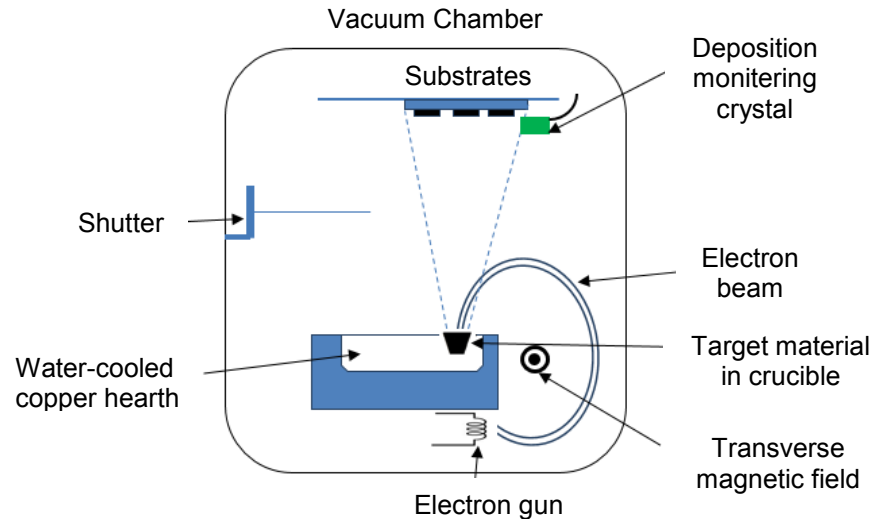
Figure 10.　*Schematic diagram of an e-beam system*

E-beam evaporation has many advantages over other PVD techniques such as controlled deposition rate (0.1 nm/min to 100 nm/min) and higher material utilization [Hu 2016]. Using e-beam deposition, films with controlled composition and microstructure, and low contamination, can be obtained. Moreover, e-beam also provides flexibility for low temperature coating on plastic substrates. In addition, multilayered and gradient coatings can be obtained [Si 2005].

One of the first borosilicate thin film using commercially available glasses was successfully deposited on polymeric substrate using e-beam in 1976 [Ad 1976]. Chi also used e-beam deposition technique to encapsulate Be-implanted InP with borosilicate glass thin films [Ch 1994]. Later, amorphous hydroxyapatite ($Ca_{10}(PO_4)_6(OH)_2$) was successfully deposited using e-beam for biomedical applications using carefully controlled deposition parameters in the e-beam evaporator and specially prepared targets prepared from hydroxyapatite powder [Ha 2001].

2.5.2 Fiber waveguides

Optical fiber is a special type of waveguide, which consists of a cylindrical glass core surrounded by a cladding made up of a lower refractive index material, which ensures the light confinement within the core. Professor Bram van Heel made first structured optical fiber in 1954 [He 1954]. To protect the fiber from fractures it is coated with a layer of

acrylate polymer or polyimide. In addition, commercial fibers have tough resin buffer layer, strength member and a jacket to insure the protection of the fiber. Schematic diagram of an optical fiber is shown in **Figure 11.**
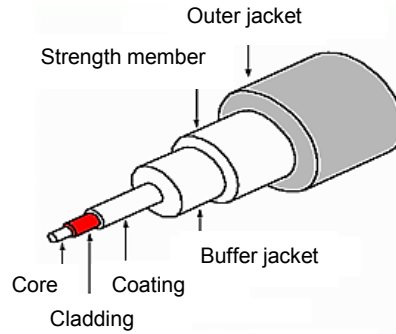
Figure 11. *Schematic diagram of a multimode optical fiber [Ad 2016]*

An optical fiber can confine either single or multiple numbers of modes of light in its core. So-called V-number, which is defined by the radius of the fiber core and the NA of the fiber gives number of allowed mode of transmission [Ag 2001].

$$V = k_0 a (n_1^2 - n_2^2)^{1/2} \qquad (3)$$

where, $k_0 = \frac{2\pi}{\lambda}$, λ is wavelength of light (in nm) to be guided, a is the radius (in nm) of the core and n_1 and n_2 are the refractive indices of the core and the cladding, respectively.

In the light of equation (3), a smaller core diameter supports fewer modes. Fiber with smaller core will support only a single pathway for light and is called a single-mode fiber whereas, a large core allows multiple input signals and provide multiples pathways for light. The core of single mode fiber is usually <10 μm while the core diameter for multimode fiber can be as high as 100 μm.

Single-mode fibers are used as a backbone to longer distance signal transfer because of no modal dispersion i.e., there is less attenuation and signals are able to travel further. The modal dispersion is distortion in the signal due to different velocities of different modes. However, because of the lower operating cost and easy handling, multi-mode fibers are useful for short connections in network [Ad 2016]. Single-mode optical fibers are commonly used when high transmission bandwidth is required in long-distance optical communications [Gh 1998].

Optical fiber can be fabricated in two steps; first, a large diameter preform needs to be prepared with core and clad structure and then the preform is heat-treated to the softening temperature of the (core and clad) glasses and pulled to form a long and thin fiber. Silica preforms are processed using vapor deposition. As sescribed in [Ma 1980], in a modified chemical vapor deposition (MCVD), a hollow glass tube is used to deposit required glass

material in inner wall of the tube by injecting silicon tetrachloride ($SiCl_4$) with oxygen from one end whereby the reaction between silicon tetrachloride and oxygen leads to the formation of silicon oxide particles. For every layer, the composition of gas can be changed to get different index profile in the preform.

Preforms can also be prepared using melting process. Different techniques can be used to prepare a core-clad preform. In extrusion method, core melt is pressed into cladding melt [Le 2007]. While in crucible method core raw material is melted in an ampoule sealed at the bottom which serves as a cladding [Go 2005]. Similarly in a core suction method, molten core material is drawn inside a cladding tube [Go 2006]. Rotational caster method is described in [Ma 2009], where the core and clad materials are prepared individually. The clad melt is first poured in a preheated mold fitted on a table as shown in **Figure 12a**. The table is quickly turned horizontally and roated at about 1000 rpm for few seconds which creates a cylindrical space inside the clad. Then core melt is slowly added and allowed to solidify. Finally the core-clad preform is annealed. Schematic diagram for the sequential steps of preform casting is illustrated in the **Figure 12b**.
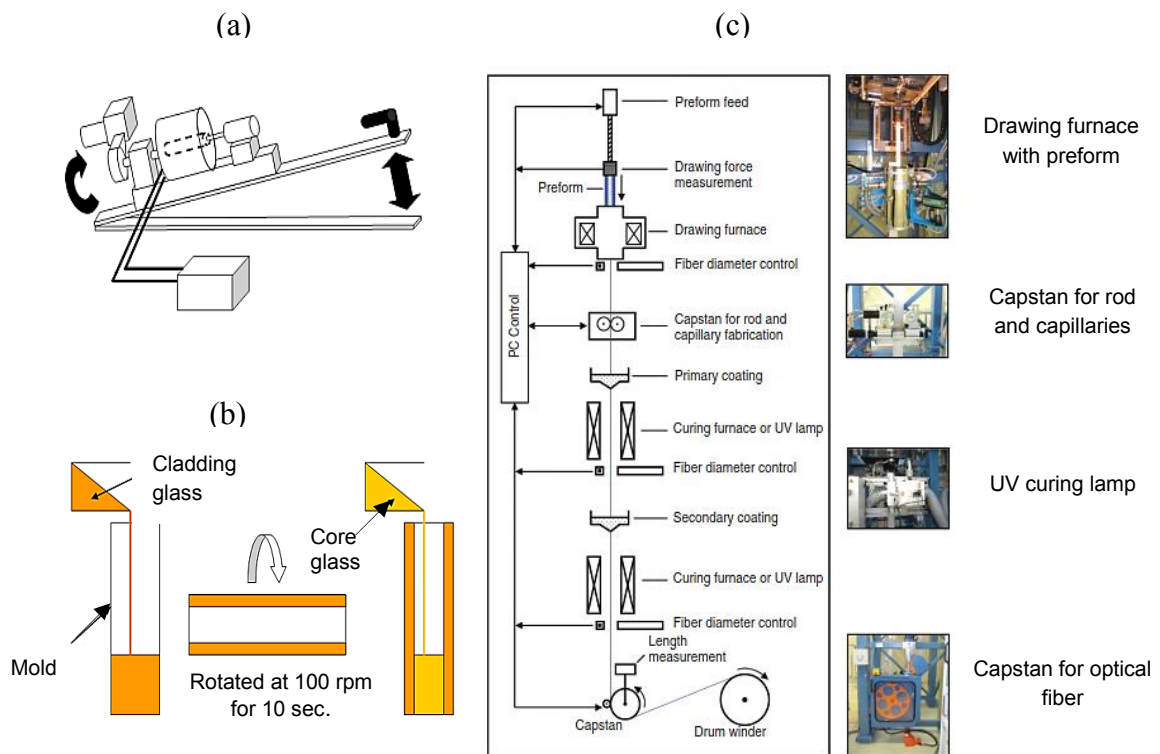
Figure 12. *Rotation cast rig (a) and sequential steps for rotational casting of preforms (b) [Ma 2009] and fiber drawing tower (c) [Sc 2014]*

Fibers from the larger preform made from any of the above mentioned methods are drawn typically in a vertical drawing process as shown in **Figure 12c**, which consists of different functional components. A high-temperature furnace in the upper part of the system is used to heat preform close to the softening temperature of the (core and clad) glasses. Preform is slowly fed through the furnace and a fiber-pulling capstan draws fiber in much faster

rate. In addition, there are coating and curing components to coat a fiber. Diameter is monitored by non-contact laser after it leaves the furnace and after coating.

2.5.3 Glass requirements

In order to fabricate an Yb−Er codoped (planar or fiber) waveguide, the glass should dissolve large amount of rare-earth elements (Yb and Er) , and should be easily processable using available standard techniques. Furthermore, to be considered as suitable candidates for thin-film deposition and/or for fiber drawing from preform, the glass must have a good thermo-mechanical resistance to casting (shock, fracture) and a good stability against crystallization. As reported in [Ma 2010], the resistance of the glass to crystallization is usually estimated by measuring the bulk glass' thermal properties such as its glass transition temperature, T_g and crystallization temperature, T_x The difference between these values, $\Delta T = T_x - T_g$, provides a gauge of the glass' resistance to crystallization. ΔT should be as large as possible. Typically a ΔT value larger than 100°C suggests reasonable glass stability.

3. METHODOLOGY

3.1 Material Processing

3.1.1 Glass preparation

Different glasses with the system $(98-x-y)(0.50P_2O_5-0.40SrO-0.10Na_2O)-0.5Er_2O_3-1.5Yb_2O_3-xZnO-yY_2O_3$ (in mol%) with x = 2.5, 5 and 10 (labeled 2.5Zn, 5Zn, 10Zn, y=0) and y = 1.25, 2.5, 3.75 and 5 (labelled 1.25Y, 2.5Y, 3.75Y and 5Y, x=0) were prepared using a standard melting method in air. The glass with x = 0 and y = 0 is labeled as REF.

$NaPO_3$, $SrCO_3$, $(NH_4)_2HPO_4$, Yb_2O_3, Er_2O_3, Y_2O_3 and ZnO were used as raw materials for the batch preparation. $Sr(PO_3)_2$ was separately prepared from the mixture of $SrCO_3$ and $(NH_4)_2HPO_4$ using slow heating rate up to 850°C. 10 gram batches were mixed in a mortar and melted in platinum crucible for 30 min between 1150°C (for the REF glass) to 1525°C, depending on the glass composition. To ensure the homogeneity of the molten glass, the glass melt was mixed before quenching. After quenching, the glasses were annealed at 400°C, ~40°C below their respective glass transition temperature for 4 hours to release stress from the quench. Finally, the glass samples were polished.

3.1.2 Film deposition

25 gram batch of REF glass ($49P_2O_5-39.2SrO-9.8Na_2O-0.5Er_2O_3-1.5Y_2O_3$ (x and y=0)) was melted using the standard melt quenching method explained in the previous paragraph. The glass melt was casted into 2.5 cm × 2.5 cm × 1 cm bulk. After quenching, the preform was annealed at 500°C for 10 hours. After annealing, the glass was cut into smaller cubes of 0.5 cm × 0.5 cm × 0.5 cm, which were cleaned with acetone and loaded into the evaporator in a tantalum crucible without further treatment.

The films in this study were deposited on silicon and quartz substrates using custom-built e-beam system (Instrumentti Mattila) equipped with tungsten filament (Telemark Model ST). The vacuum was pumped by a turbo pump and a back pump, reaching vacuum pressure of ~10^{-5} mbar. Prior to deposition, the substrates were ultrasonically cleaned in acetone and isopropanol for 10 minutes. To insure no dust particles on the substrate, the substrates were blown by nitrogen prior to loading. Substrates were heated with halogen flash lamps to 110°C in the vacuum and deposition was done using 5, 9, 13 and 21 mA for 45 minutes each. The acceleration voltage was 9kV and the pressure varied from 4.8 to 4.0x10^{-5} Torr. The electron beam was manually scanned over the target to get uniform melting. All the depositions were performed using fresh targets. After each deposition, some of the films were annealed at 225°C for 5 hours while the others were

kept in the nitrogen environment. Images of the surface of the film were taken using an optical microscope right after the deposition and after aging.

3.1.3 Fiber drawing

25 gram batch of REF glass ($49P_2O_5$-$39.2SrO$-$9.8Na_2O$-$0.5Er_2O_3$-$1.5Y_2O_3$ (x and y=0)) was melted using the standard melt quenching method (see section 3.1.1) and casted into a single core preform with 1 cm diameter and 10 cm length in a graphite mold preheated at 300°C. After quenching, the preform was annealed at 400°C for 10 hours. The cylindrical preform was polished and sent to Rennes University in France for fiber drawing.

Fibers with average diameter of 115$\pm$1 μm were drawn in a fiber drawing tower as described in section 2.5.2. Drawing temperature was 550°C and the furnace was purged with Helium gas to create inert atmosphere around the preform. The fiber was drawn at a speed of ~10 mm/min with preform insertion speed of 2 mm/min. As-drawn fiber was left uncoated to perform thermal and structural characterizations.

3.2 Composition Analysis

A scanning electron microscope (Carl Zeiss Crossbeam 540) equipped with Oxford Instruments X-Max[N] 80 EDS detector was used to image and analyze the composition of the samples. The polished glasses were coated with a thin carbon layer before EDS mapping. The accuracy of the elemental analysis was $\pm$ 1.5 mol%.

Schematic diagram of Scanning electron microscopy (SEM) and the interaction volume created by electron sample interaction is presented in **Figure 13**.
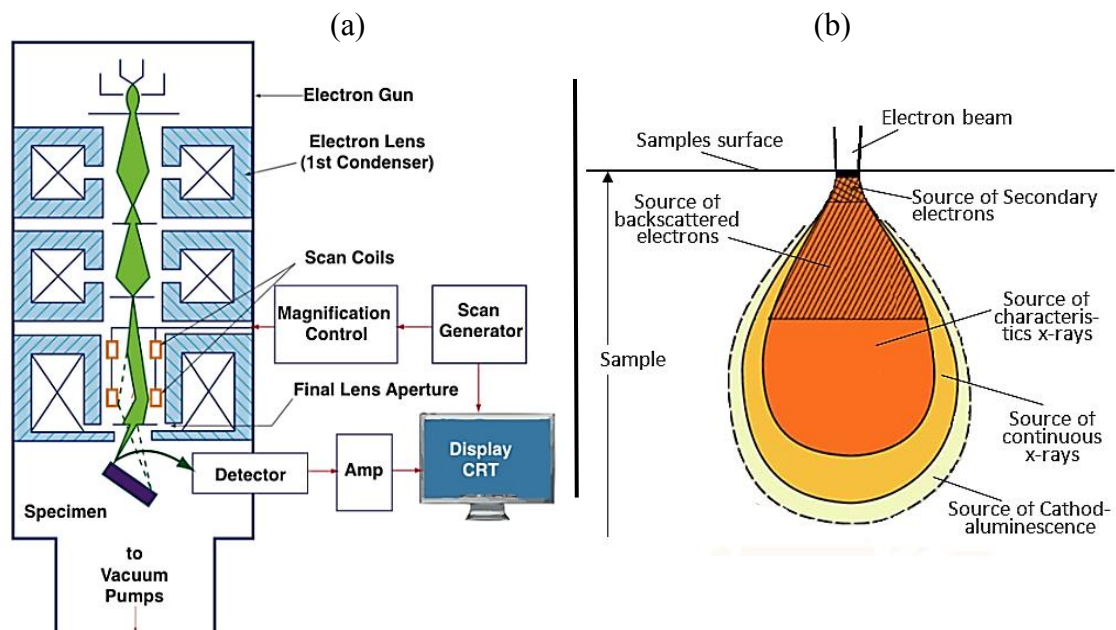
Figure 13. *Schematic diagram of SEM (a) and interaction volume (b) [Go 2007]*

According to [Go 2007], SEM is a non-contact, non-destructive technique for imaging surface topography. It consists of an electron gun for electron emission and different electron lens system that direct the e-beam down towards the sample through high vacuum tube. SEM imaging begins with the electron emission from the gun (**Figure 13a**). This electron beam is aimed towards the specimen through an aperture and magnets are used to change its size and shape. When the electron beam hits the surface of the specimen, the electrons will penetrate the surface creating an "interaction volume" (**Figure 13b**) whereby the secondary electrons, backscattered electrons, and characteristic X-rays are emitted. Backscattered and secondary electrons carry information on the specimen composition, topography, surface texture, thickness etc. SEM can also determine the structural features deeper under the surface from the characteristic X-rays produced in the deeper part of interaction volume.

X-rays are produced when an electron from an atom is knocked out and the vacant orbital is filled by the electron transition from higher orbitals with the emission of characteristic radiation. The energies of electron shells vary in discrete manner with atomic number, so the emitted radiations have energies characteristic of that atom. The energy of the characteristic radiation within a given series of lines varies monotonically with atomic number and is given by Moseley's Law [Go 2007].

According to Moseley's law,

$$E = A(Z - C)^2 \tag{4}$$

where, E is energy of the emission line for a given X-ray series in KeV, Z is atomic number and A and C are constant that depends upon the type of X-ray lines.

Moseley's law forms the basis for elemental analysis with EDS. If the energy of a given K, L or M line is measured, then the atomic number of the element producing that line can be determined [Go 2007].

3.3 Physical and thermal properties

The density of the glasses was measured by Archimedes' principle which states that 'a body immersed in fluid loses weight equal to the amount of fluid it displaces'. The density was calculated using equation (5).

$$\rho_{sample} = \frac{W_a}{W_a - W_l} \rho_{liquid} \tag{5}$$

where, W_a and W_l are the weight of sample measured in air and water respectively. ρ_{sample} and ρ_{liquid} are density of glass and the density of immersion liquid respectively.

The density of bulk glass material was measured using ethanol as an immersion liquid and a digital weight equipped with density measurement kit. The accuracy of measurement was ±0.02 g·cm^{-3}.

The glass transition and crystallization temperatures of the bulk glasses and fiber were analyzed via Differential Thermal Analysis (DTA) using NETZSCH STA 449. A typical DTA thermogram is presented in **Figure 14**.
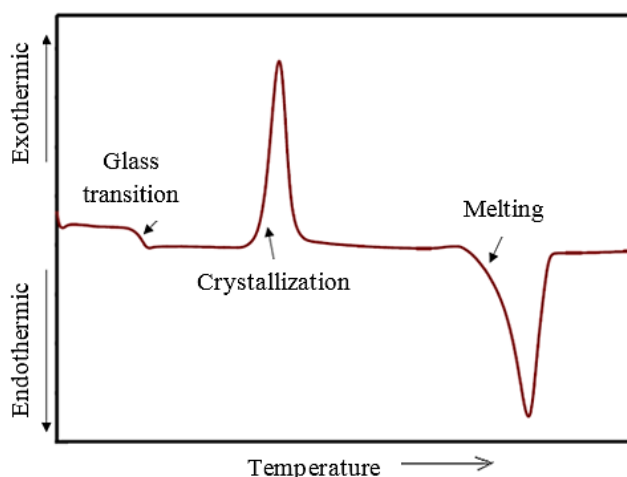
Figure 14. *Typical DTA thermogram showing change of heat flow as a function of temperature*

DTA is a thermal analysis technique in which zero temperature difference is established between a sample and an inert reference [Bh 2002]. Two specimens are heated in a furnace and the enthalpy changes in the sample associated with absorption or evolution of heat cause the change in differential heat flow. The area under the peak is directly proportional to the enthalpy change and its direction indicates whether the thermal event is endothermic or exothermic. The heat flow of the sample is plotted as a function of temperature.

At glass transition temperature (T_g), the glass network starts to break releasing energy and becomes more free to rotate. However, at the crystallization temperature, the glass forms intermolecular bonds in expense of heat and attains more orderly arrangements. Similarly, melting starts with the breaking of intermolecular bonds and is represented by the onset of endothermic curve.

Glasses were crushed into fine powder and (30.000 ± 0.025) mg was weighed into a platinum pan. Samples were analyzed in a nitrogen atmosphere, using a platinum reference, and sapphire disc were placed in between the machine head and crucible. The glass transition temperature (T_g) and the crystallization temperature (T_x) were recorded at a heating rate of 10 K/min between 30 to 800°C. T_g was taken at the inflection point of the endotherm, as obtained by taking the first derivative of the DSC curve. The onset (T_x) and the peak (T_p) crystallization temperatures were taken at the inflection point and the highest

point of first exothermic peak, respectively. All the characteristic temperatures were obtained with an accuracy of ±3°C.

3.4 Optical properties

3.4.1 Optical properties of bulk glasses

The absorption spectra of the bulk glasses were measured using UV-VIS-NIR spectrophotometer (UV-360 Plus, Shimadzu) from 200 to 1750 nm with the resolution of 0.5 nm. A schematic diagram of a double beam spectrophotometer is shown in **Figure 15**.
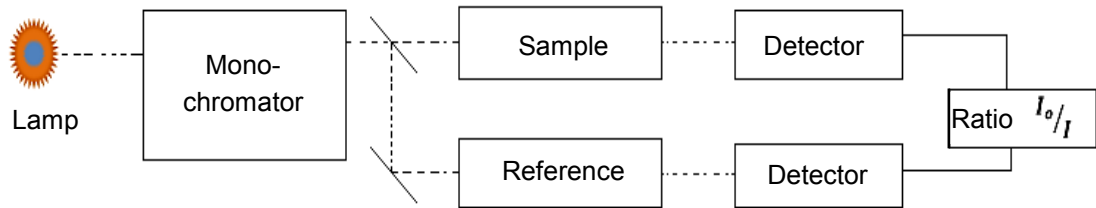
Figure 15.   *Schematic diagram of two beam spectrophotometer*

The reference beam passes through free medium and its intensity is recorded as I_o whereas the beam passing through sample has intensity I. A spectrometer produces a range of wavelengths for scanning and the photometer records the number of photons being emitted after absorption. Absorbance is calculated on the basis of ratio (I_o/I).

$$A = \log(I_o/I) \tag{6}$$

where, A is the absorbance.

The absorption coefficient is calculated from the Beer Lambert law using equation (7).

$$\alpha = \frac{2.302585}{L} \log(I_o/I) \tag{7}$$

where, L is thickness of the sample (cm).

The absorption cross-section $\sigma_{abs}(\lambda)$ is calculated using equation (8).

$$\sigma_{abs}(\lambda) = \frac{\ln 10}{NL} \log(I_o/I) \tag{8}$$

where, N is the rare-earth ion concentration (ions·cm⁻³) calculated from the batch composition and glass density. The accuracy of absorption cross-section measurement was ±10%.

3.4.2 Attenuation in fiber

Transmission loss is the main characteristic of guided light. Loss in fiber is mainly due to attenuation losses, which is caused by the absorption and scattering of light. Absorption may include atomic transition in UV and molecular vibration in the IR wavelength region or due to the water molecules or OH bond absorption. Scattering occurs due to the microscopic variations in the material density, compositional fluctuations, structural inhomogeneity and manufacturing defects. As stated in [Fr 2000], when the size of scattering inhomogeneities is less than one tenth of the wavelength of the incident light, it is called Rayleigh scattering whereas scattering centers larger than one tenth of wavelength of incident light produce Mie scattering. According to transmission, fiber loss is expressed as

$$Loss = A\lambda^{-4} + B(\lambda) + C \tag{9}$$

where, A is constant for Raleigh scattering loss, B is constant for wavelength dependent losses such as UV and IR absorptions and C includes wavelength independent losses like imperfection in waveguide.

The attenuation in fiber is the reduction in signal strength and is obtained by comparing output power (P_{out}) to the input power (P_{in}). It is measured in logarithmic scale as,

$$\alpha(dB) = -10 \times (P_{out}/P_{in}) \tag{10}$$

Losses were measured using the cutback method in custom-built setup as shown in **Figure 16**. Cut back method involves comparing the optical power transmitted from a longer piece of fiber to that of shorter piece.
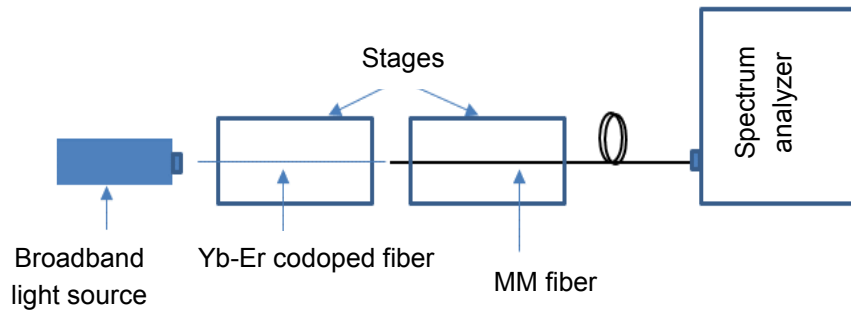

Figure 16. *Schematic diagram for fiber loss measurement*

A broadband light (400-2400 nm) was used as an input source at one end of fiber and output power at the other end was collected by coupling it with a multimode fiber (AFS 105/125Y). The attenuation spectrum of the output was measured by an optical spectrum analyzer (Ando, AQ-6315A). The resolution of the spectrum was 0.5 nm.

3.5 Spectroscopic Properties

Emission of fiber and bulk glasses in NIR region was recorded using a custom-built setup as described in **Figure 17**. The fiber/bulk glass was pumped using a 975 nm laser diode (Oclaro, China). Isolator prevented the backflow of laser and the light was collimated using a high power lens (f = 4 mm). Light was launched at one end of fiber and emitted light was collected at the other end using a multimode fiber. Emission Spectra were obtained in 400-1700 nm range by an optical spectrum analyzer.
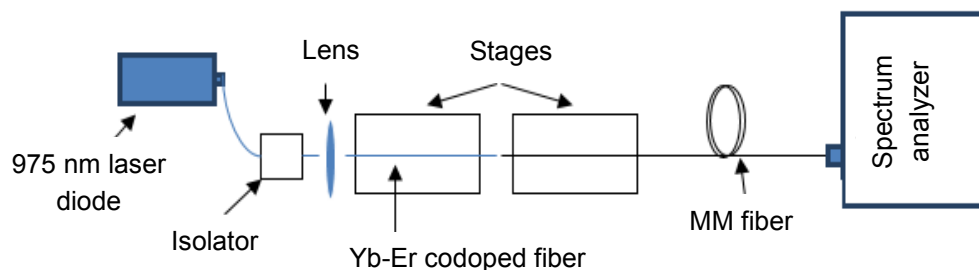
Figure 17. *Schematic diagram for emission measurement*

3.6 Structural Properties

The structural properties of the glasses were measured using IR and Raman spectroscopies.

3.6.1 Infrared Spectroscopy

The IR spectra were measured using a 'Perkin Elmer Spectrum one FTIR spectrometer' in Attenuated Total Reflectance (ATR) mode in mid-infrared region 600-1400 cm^{-1}. The resolution used was 2 cm^{-1} and the spectra were obtained from the accumulation of 8 scans.

Infrared spectrum is related to vibrational energy level of the molecule and thus gives structural information of molecules in sample. Every molecule absorbs the infrared radiation that causes the change in its dipole moment and the vibrational energy level is transferred to an excited state. The number of the absorption bands is related to the number of vibrational freedom of the molecule. The intensity of absorption bands is related to the change of dipole moment. The infrared absorption spectroscopy works under the principle of Michelson interferometer. The infrared interferogram is obtained in the time domain from the interference of light from the fixed and the movable mirror. This time domain is Fourier transformed to frequency domain to get meaningful spectrum (Fourier Transformed Infrared Spectroscopy). **Figure 18** depicts the interferogram of polychromatic light (a) and its Fourier transformed spectrum (b).
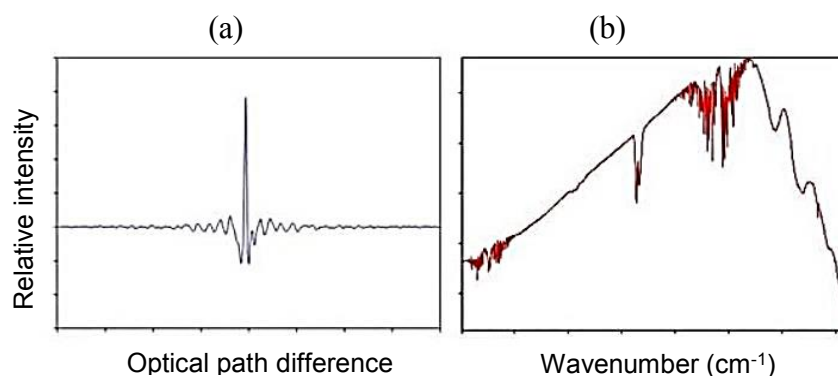
Figure 18. *Interferogram of a monochromatic light (a); its spectrum (b) [LibreTexts]*

3.6.2 Raman Spectroscopy

The Raman spectra of the samples were measured using Thermo Scientific™ DXR™ 2xi Raman imaging microscope. The wavelength of the laser was 532 nm and the power at the sample was 2.0 mW. The exposure time was 0.2 seconds per pixel and data was averaged four times.

Raman spectrum is due to the inelastic scattering of photons and relies on change in polarizability of a molecule. The sinusoidal vibration of molecule changes the polarization of a molecule and the photon loses or gains energy that is equal to the vibrational energy of the molecule [Ba 2001]. Schematic diagram of Raman spectra measurement the principle of Raman spectroscopy is shown in **Figure 19**.
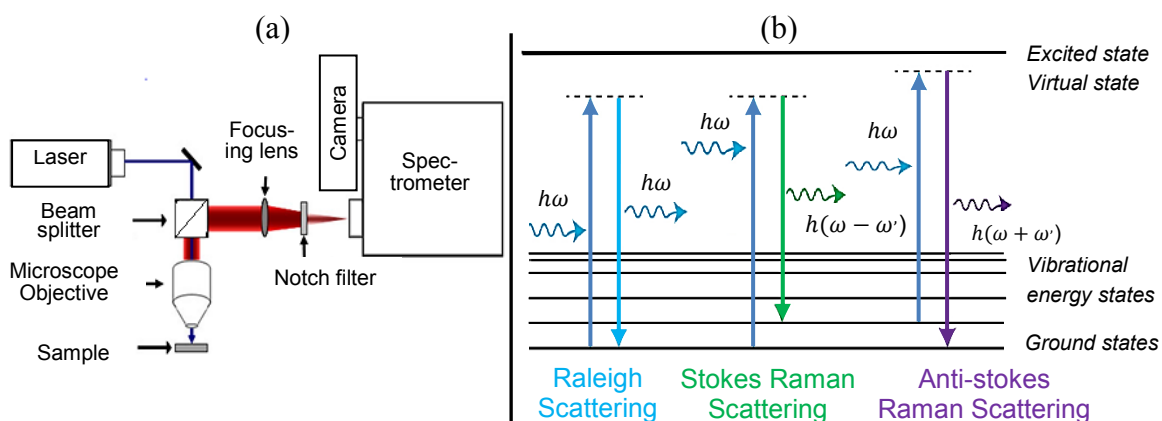
Figure 19. *Schematic diagram of Raman spectra measurement (a) and principle of Raman spectroscopy (b)*

As described in [Ho 2004], when laser light excites the vibrating molecule, it jumps to some virtual state. The excited molecule returns to the ground state with release of same amount of energy (Raleigh scattering) or to different states energy states with higher or lower frequency photons (Raman scattering). Raleigh scattering, which is dominant, is filtered out and only Raman signals are analyzed via spectrometer.

3.7 XRD Analysis

X-ray diffraction (XRD) is a material characterization technique that is used to determine the crystalline quality, chemical composition, and atomic structure of a solid material. The crystalline phases of target were identified using an X-ray diffraction analyzer with Cu Kα_1 radiation (λ = 1.5406 Å). Data was collected from 2Θ = 10°-90° in 0.013° intervals.

Wavelength of X-rays are similar in size to the interatomic spacing (d_{hkl}) of almost all the elements in periodic table thus the periodic and regular arrangements of atoms in crystal diffract X-ray strongly in the direction governed by the Bragg's diffraction law [He 2009]. According to Bragg's law, X-rays scattered from the successive planes of a crystal will constructively interfere if the path difference between the diffracted rays is equal to an integer multiple of the wavelength (nλ). Bragg's law can be written as:

$$2d_{hkl}Sin\theta = n\lambda \tag{11}$$

where, n is an integer, λ is the wavelength of the incident x-ray measured in nm, d_{hkl} is the spacing between the planes in the atomic lattice in Å, and θ is the angle in degrees between the scattered wave and the atomic plane.

Schematic diagram of X-ray diffraction in a crystal lattice with atomic spacing d_{hkl} is shown in **Figure 20a**. In X-Ray spectrometer, a divergent x-ray from the tube is incident on sample that passes through different slits and filters as shown in **Figure 20b**. The detector collects the diffracted beam from the sample, which is placed at an angle 2Θ with the incident beam. Detector and tube can be moved along the goniometer circle.
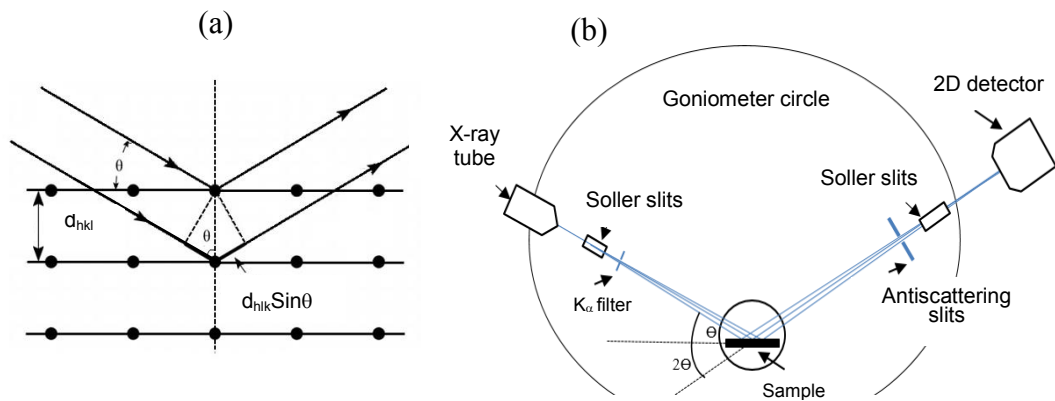
Figure 20.   *Diffraction of X-ray by a crystal lattice (a) and X-Ray spectrometer (b)*

A plot of the diffraction pattern for a crystal as a function of the incident angle will result in a spectrum characteristic of the crystal structure. The angular position of the peaks will give an indication of the lattice parameters [He 2009].

4. RESULT AND DISCUSSION

4.1 Processing and characterization of the glasses

4.1.1 First glass series

Phosphate glasses were prepared using standard melting method in air and with 0.5 mol% Er_2O_3 and 1.5 mol% Yb_2O_3. Different concentrations of ZnO (x) and Y_2O_3 (y) were added in the glass within the glass system $(98-x-y)(0.50P_2O_5-0.40SrO-0.10Na_2O)-0.5Er_2O_3-1.5Yb_2O_3-xZnO-yY_2O_3$ in order to enhance the spectroscopic properties of the glasses.

The density and the thermal properties of the glasses are presented in **Table 2**.

Table 2. Density (ρ) and thermal properties of the investigated glasses

Sample code	x	y	ρ (gcm^{-3}) ±0.02 gcm^{-3}	T_g (°C) ±3	T_x (°C) ±3	T_p (°C) ±3	ΔT (T_x-T_g) (°C) ±6
REF	0	0	3.21	462	580	593	118
2.5Zn	2.5	-	3.23	466	576	596	110
5Zn	5	-	3.26	445	560	577	115
10Zn	10	-	3.32	444	549	570	105
1.25Y	-	1.25	3.25	465	581	597	116
2.5Y	-	2.5	3.26	448	560	580	112
3.75Y	-	3.75	3.33	483	609	622	126
5Y	-	5	3.35	494	624	645	130

An increase in the glass density with an increase in x and y can be seen. This can be linked to the partial replacement of P_2O_5, Na_2O and SrO in glass network by the heavier Zn or Y atoms. While an increase in ZnO content (x) decreases T_g, T_x and T_p, an increase in Y_2O_3 content (y) increases the glass thermal properties. The increase in T_g could indicate that the addition of Y_2O_3 improves the strength of the network, whereas Zn is suspected to act as a network modifier, in agreement with Schwarz et al. [Sc 2004]. Also shown in

the table is ΔT, the temperature difference between T_x and T_g, which is an indicator of the glass resistance to crystallization. No real impact on the addition of ZnO can be noticed on the thermal stability of the glasses. However, the addition of Y_2O_3 seems to increase the thermal stability against crystallization of the glass.

In order to understand the changes in the physical and thermal properties of the glasses induced by the addition of ZnO and Y_2O_3, the IR absorption and Raman spectra of the glasses were measured. The IR absorption spectra of the ZnO (x) and Y_2O_3 (y) containing glasses are presented in **Figure 21**. They are normalized to the main band at 880 cm^{-1}, thus all the discussed intensity changes are expressed relatively to the main band.

Figure 21. *IR absorption spectra of ZnO (a) and Y_2O_3 (b) -containing glasses*

The spectra exhibit a broad band between 650 and 800 cm^{-1}, three absorption bands located at around 1260, 1085 and 885 cm^{-1}, and a shoulder at 980 cm^{-1}. The broad band between 650 and 800 cm^{-1} can be related to symmetric vibrational modes ν_{sym} (P−O−P) of Q^2 units. The strong absorption band at 885 cm^{-1} is due to asymmetric stretching vibrational modes ν_{as} (P−O−P) in Q^2 units [Na 2015][Ra 2013]. The shoulder centered at 980 cm^{-1} and the band at 1085 cm^{-1} are due to symmetric and asymmetric stretching vibrations of Q^1 units, respectively [Na 2015]. The band at 1085 cm^{-1} can be attributed to an overlap between Q^1 units and Q^2 units in metaphosphate. The shoulder at 1160 cm^{-1} and the band at 1250 cm^{-1} are mainly due to symmetric and asymmetric vibrations of PO_2^- in Q^2 units respectively.

The progressive addition of ZnO leads to a decrease in intensity of the bands at 1085 and 1250 cm^{-1} compared to the main band whereas the addition of Y_2O_3 increases the intensity of the band at 1085 cm^{-1} and decreases the intensity of the band at 1250 cm^{-1}. A shift of all the bands towards higher wavenumbers can be also observed which is a clear sign of changes in the strength of the chemical bonds in the glass network.

The Raman spectra of the ZnO (x) and Y_2O_3 (y) containing glasses are presented in **Figure 22**. They are normalized to the band at ~1170 cm^{-1}, thus all the discussed intensity changes are expressed relatively to the main peak.
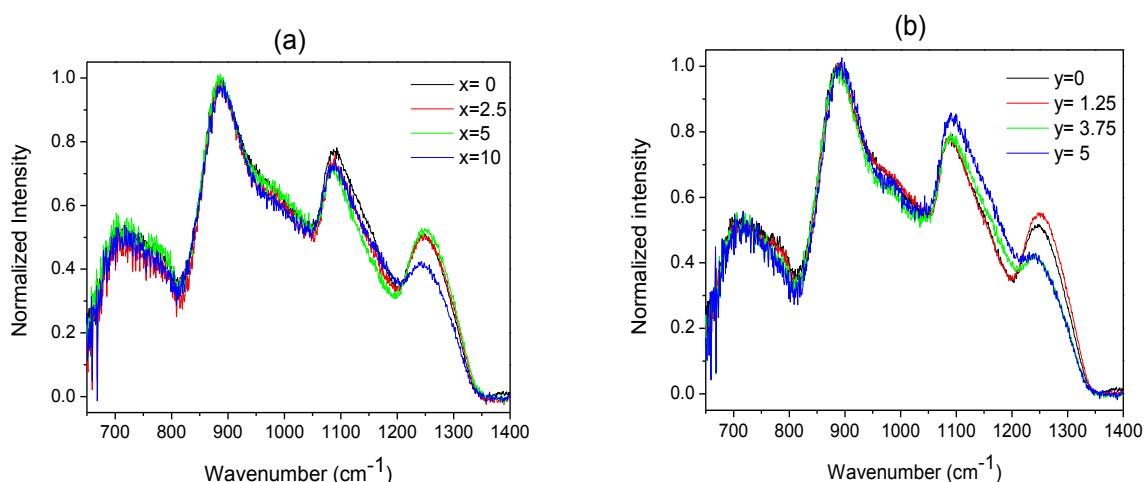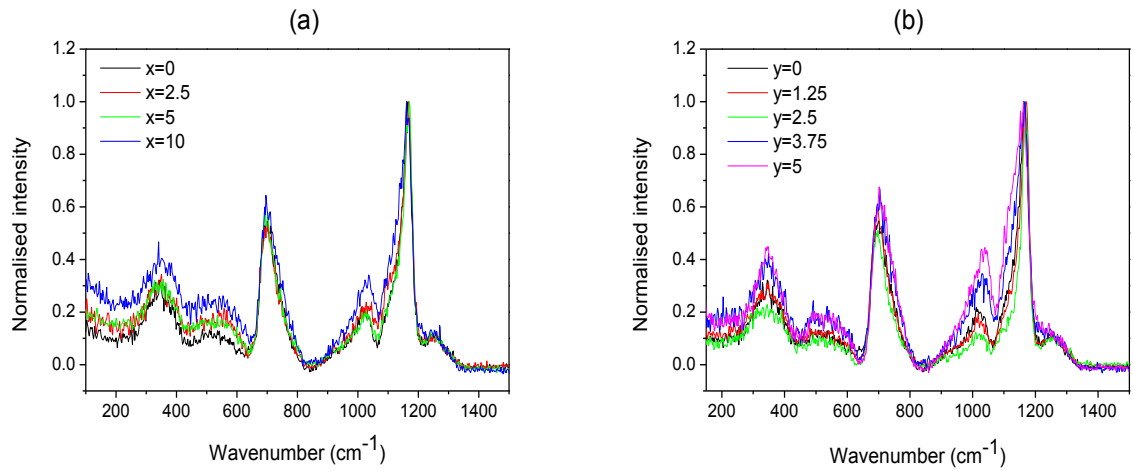

Figure 22.   *Raman spectra of ZnO (a) and Y_2O_3(b) -containing glasses*

The Raman spectra of the glasses exhibit bands at 300, 500, ~700, 1170 and 1280 cm^{-1} and several bands between 800 and 1110 cm^{-1}. The band at 300 cm^{-1} can be attributed to ZnO_4 units and the bands in the 400-600 cm^{-1} range can be related to bend mode of phosphate polyhedral and to Zn-O vibration [Li 1997]. The band centered at 700 cm^{-1} can be related to the symmetric stretching of bridging $v_{sym}(P{-}O{-}P)$ of Q^2 groups and the band at 1020 cm^{-1} to the symmetric stretching $v(P{-}O)$ of terminal Q^1 groups. The bands at ~1170 and 1280 cm^{-1} can be attributed to symmetric and asymmetric stretching of non-bridging $v(PO_2)$ of Q^2 groups respectively [Ko 2010]. With the addition of ZnO and Y_2O_3, the bands in the 200-1100 cm^{-1} range increase in intensity compared to that of the main band.

Before discussing the results, it is crucial to recapitulate the structure of a phosphate glass. As explained in Schwarz et al. [Sc 2004], in ultraphoshate glasses ([P_2O_5]>50mol%), the structural units are Q^3 and Q^2 tetrahedra, the Q^3 units forming the 3D network while the Q^2 units assist the chain formation. With a decrease in P_2O_5 content, the structure of the glass becomes metaphosphate formed by Q^2 units with chains of (P−O−P)-bridges and rings. Further reduction in P_2O_5 content leads to the formation of polyphosphate glasses formed by shorter chains of Q^2, which are terminated by Q^1 units. The IR and Raman spectra confirm the metaphosphate of our glasses' structure. The presence of the Raman bands at ~700 cm^{-1} indicates that the chains are present with different lengths. We suspect ZnO to enter as modifiers leading to a depolymerization of the network (increase of the Q^1 units at the expense of the expense of the Q^2 units). On the contrary, the increase in T_g induced by the progressive introduction of Y_2O_3 can be related to the formation of P−O−Y bonds and so to the distortion of the glass network. The change in the average length of the P−O−P bond with the addition of Y_2O_3 is confirmed by the shift of the Raman band position.

The absorption spectra of the investigated glasses are shown in **Figure 23**.
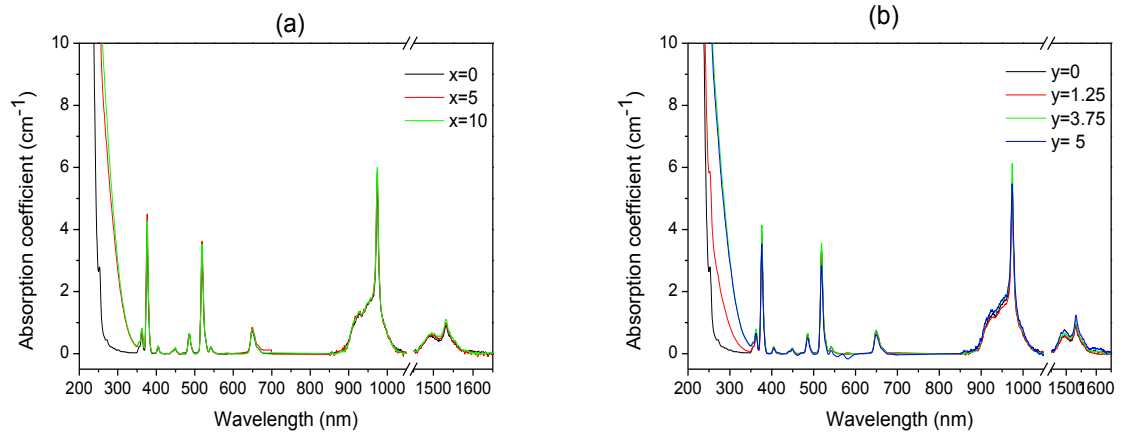
Figure 23. *UV-VIS-NIR absorption spectrum of ZnO (a) and Y₂O₃(b) -containing glasses*

The spectra exhibit several bands, which are characteristics of the Er^{3+} ion 4f−4f transitions from the ground state to various excited levels [Ba 1994]. The absorption band at 975 nm can be also related to the Yb^{3+} 4f−4f ($^2F_{7/2} \rightarrow{}^2F_{5/2}$) transition which overlaps with the weak absorption band of Er^{3+} ion. An increase in x and y leads to a shift of the band gap to longer wavelength probably due to the depolymerization of the phosphate network and/or to the formation of non-bridging oxygen as discussed in the previous paragraph. The absorption cross-section at 975 nm and 1.5 μm were calculated from the absorption coefficient using equation (7) and are presented in **Table 3**.

Table 3. *Optical properties of ZnO and Y₂O₃ containing glasses*

Sample code	x	y	$[\boldsymbol{Er^{3+}}]$ ($\cdot 10^{20}$) (ions·cm⁻³) ±5%	$[\boldsymbol{Yb^{3+}}]$ ($\cdot 10^{20}$) (ions·cm⁻³) ±5%	Absorption coefficient (cm⁻¹)		Absorption cross-section ($\boldsymbol{\sigma_{abs}}$) ($\cdot 10^{-21}$) (cm²) ±10%	
					975 nm	1.5 μm	975 nm	1.5 μm
REF	0	0	1.58	4.75	5.26	0.92	8.30	5.79
2.5Zn	2.5	-	1.58	4.73	5.38	1.01	8.53	6.41
5Zn	5	-	1.60	4.81	5.85	1.00	9.13	6.23
10Zn	10	-	1.66	4.97	6.00	1.10	9.06	6.63
1.25Y	-	1.25	1.56	4.67	5.09	0.94	8.17	6.05
2.5Y	-	2.5	1.54	4.63	5.46	1.04	8.83	6.73
3.75Y	-	3.75	1.56	4.69	6.12	1.10	9.80	7.08
5Y	-	5	1.55	4.66	5.47	1.24	8.80	7.96

Within the accuracy limit, no variation in the absorption cross-section at 975 nm and at 1.5 μm can be observed with an increase in x and y indicating that the sites of the Er^{3+} and Yb^{3+} ions are not strongly affected by the change in the glass composition. Er^{3+} and Yb^{3+} ions are thought to be surrounded mainly by P, Na and Sr.

The emission spectra of the glasses were measured using a 975 nm pumping. No noticeable increase in the intensity of emission at 1.5 μm was observed in agreement with the absorption cross-section at 975 nm presented in **Table 3**. The normalized emission spectra of the prepared glasses under 975 nm excitation wavelength are displayed in **Figure 24**.
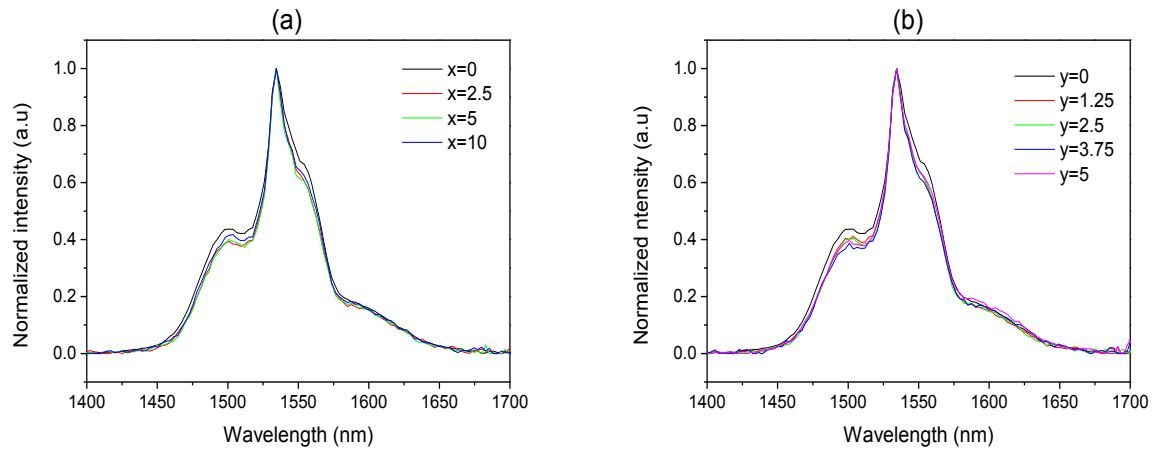
Figure 24.   *Normalized emission spectra of ZnO (a) and Y₂O₃ (b) -containing glasses*

An increase in the concentration of ZnO and Y_2O_3 leads to small changes in the shape of the emission band confirming that Er^{3+} and Yb^{3+} ion's sites are not strongly affected by the changes in the glass composition.

4.1.2 Second glass series

A second glass series was prepared with y = 1.25 and 2.5 and using different Er_2O_3 and Yb_2O_3 content in order to increase the spectroscopic properties of the glasses. The melting temperature was increased to 1500ºC to be able to melt the glass batches. **Table 4** lists the composition of the new glasses as well as their density and thermal properties.

Table 4.   Density and Thermal properties of glass series with y = 1.25 and y = 2.5

Sample code	Y_2O_3	Er_2O_3	Yb_2O_3	ρ (g·cm^{-3}) ±0.02 g·cm^{-3}	T_g (°C) ±3	T_x (°C) ±3	T_p (°C) ±3	ΔT (T_x-T_g) (°C) ±6
1.25Y0.5-1.5	1.25	0.5	1.5	3.25	465	581	597	116
1.25Y1-3	1.25	1	3	3.43	490	623	640	133
1.25Y1.5-4.5	1.25	1.5	4.5	3.59	520	651	688	131
1.25Y1.5-6.8	1.25	1.5	6.8	3.80	547	658	680	111
2.5Y0.5-1.5	2.5	0.5	1.5	3.26	448	560	580	112
2.5Y1-3	2.5	1	3	3.43	490	627	646	137
2.5Y1-4.5	2.5	1	4.5	3.62	533	657	676	124
2.5Y1.5-4.5	2.5	1.5	4.5	3.60	547	673	685	126

A clear increase in the density of glass with an increase of Er_2O_3 and Yb_2O_3 content is seen because of the partial replacement of P_2O_5, Na_2O and SrO in glass network by the heavier rare-earth atoms. Similarly, there is an increase in T_g and T_x with increased Er_2O_3 and Yb_2O_3 concentrations. With increase in the rare-earth ions, the glass structure is getting stronger whilst maintaining the resistance to the crystallization, as illustrated by the Δ*T*, which is larger than 100°C for all glasses.

As performed for the first glass series, the absorption coefficient and cross-sections for the second glass series were measured. An increase in the Er_2O_3 and Yb_2O_3 content leads to a significant increase in the absorption coefficient at 975 and 1550 nm but has no impact on the absorption cross-section at 975 and 1550 nm. Numerical values of absorption coefficient and cross-sections are listed in the **Table 5**.

Table 5. Optical properties of second series glasses

Sample code	y	Er$_2$O$_3$	Yb$_2$O$_3$	$[Er^{3+}]$ ($\cdot 10^{20}$) (ions·cm^{-3}) ±5%	$[Yb^{3+}]$ ($\cdot 10^{20}$) (ions·cm^{-3}) ±5%	Absorption coefficient (cm^{-1})		Absorption cross-section (σ_{abs}) ($\cdot 10^{-21}$) (cm^2) ±10%	
						975 nm	1.5 μm	975 nm	1.5 μm
1.25Y0.5-1.5	1.25	0.5	1.5	1.56	4.67	5.09	0.94	8.17	6.05
1.25 Y 1-3	1.25	1	3	3.15	9.45	9.90	2.08	7.86	6.60
1.25 Y 1.5-4.5	1.25	1.5	4.5	4.75	14.2	14.10	2.97	7.43	6.26
1.25 Y 1.5-6.8	1.25	1.5	6.8	4.81	21.8	17.62	3.03	6.63	6.30
2.5Y0.5-1.5	2.5	0.5	1.5	1.54	4.63	5.46	1.04	8.83	6.73
2.5 Y 1-3	2.5	1	3	3.12	9.35	9.18	1.92	7.36	6.16
2.5 Y 1-4.5	2.5	1	4.5	3.19	14.4	13.34	2.06	7.61	6.46
2.5 Y 1.5-4.5	2.5	1.5	4.5	4.71	14.1	13.08	2.95	6.94	6.26

While no significant variation in absorption cross-section at 1.5 µm was measured for the new glass series, clear changes in shape of the absorption band at 975 nm is seen in **Figure 25**. This shows that addition of higher concentration of RE dopants have some effect on absorption band especially at the lower wavelength side.
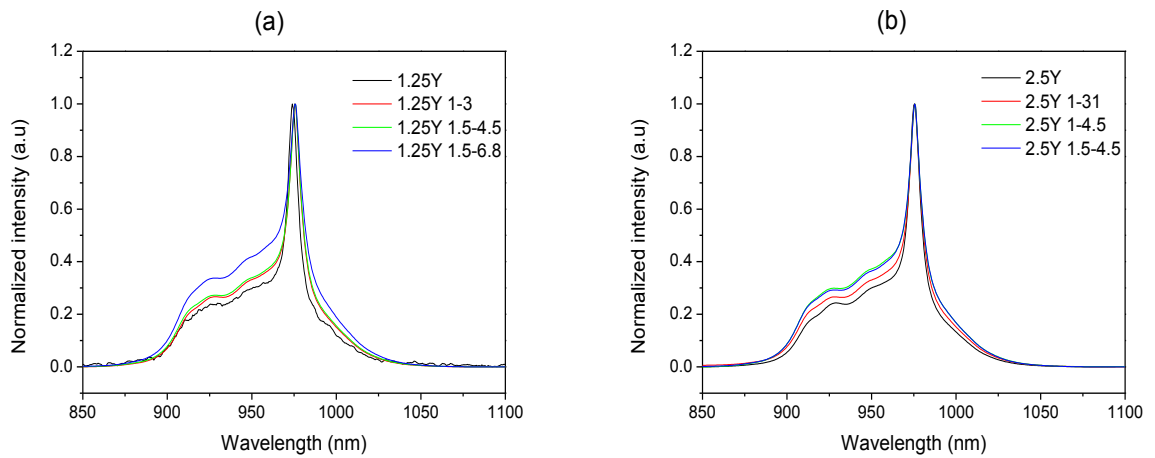

Figure 25. *UV-VIS-NIR absorption spectrum at 975 nm for second glass series*

4.1.3 Glass selection for waveguide fabrication

Based on the thermal, optical and spectroscopic properties of the glasses, the glasses with the code 1.25Y1.5-6.8 and 2.5Y1.5-4.5 seem to be good candidates to be deposited into thin films and to be drawn into fibers. However, target (25 gram block) and preforms (1 cm diameter and 10 cm long rod) need to be prepared for film deposition and fiber drawing, respectively. Because of the high melt viscosity and the high melting temperature of the glass melts with the composition 1.25Y1.5-6.8 and 2.5Y1.5-4.5, thin film and fiber were fabricated from the reference glass with the composition $49P_2O_5$-$39.2SrO$-$9.8Na_2O$-$0.5Er_2O_3$-$1.5Yb_2O_3$.

4.2 Planar waveguide: Thin film using e-beam deposition

For film deposition, 25 gram of glass was prepared. The glass melt was casted into 2.5 cm × 2.5 cm × 1 cm bulk and annealed at 400°C for 10 hours. After annealing, the glass was cut into smaller cubes of 0.5 cm × 0.5 cm × 0.5 cm. Each piece was cleaned with acetone and loaded into the evaporator in a tantalum crucible without further treatment. Films were deposited on quartz and silicon slides using current from 5 to 21 mA. The thickness, measured using a SEM by taking the cross-sectional images of the film, was found to increase from ~0.5 μm to ~3.2 μm when the current was increased from 5 and 21 mA. Films were annealed right after the deposition at 225°C for 5 hours in air. The duration of the deposition was 45 minutes.

We noticed that the glass target needed to be replaced after each deposition trail as it became milky after e-beam deposition independently of the current as shown in **Figure 26** below.

(a)   (b)
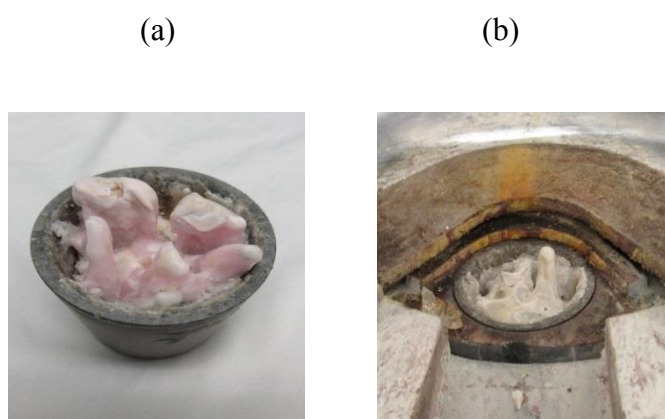
Figure 26. *Images of target after deposition with deposition current 9 mA (a) and 21 mA (b)*

Figure 27 shows some SEM pictures of the targets after deposition using 5 and 9 mA, taken as an example.
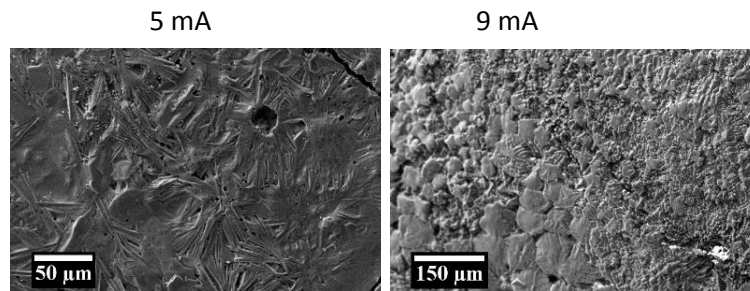
Figure 27. *SEM images of the targets after deposition at 5 and 9 mA*

Independently of the current, all crystals with needle like shape were clearly observed in the target. In order to confirm and identify the crystalline phases precipating in the target during the deposition, the remaining targets after deposition were crushed into powder and the XRD patterns were measured using an X-ray diffraction analyzer. **Figure 28** presents the XRD pattern of the target after deposition using 9 mA taken as an example as the XRD patterns of 4 targets were found to be the same.
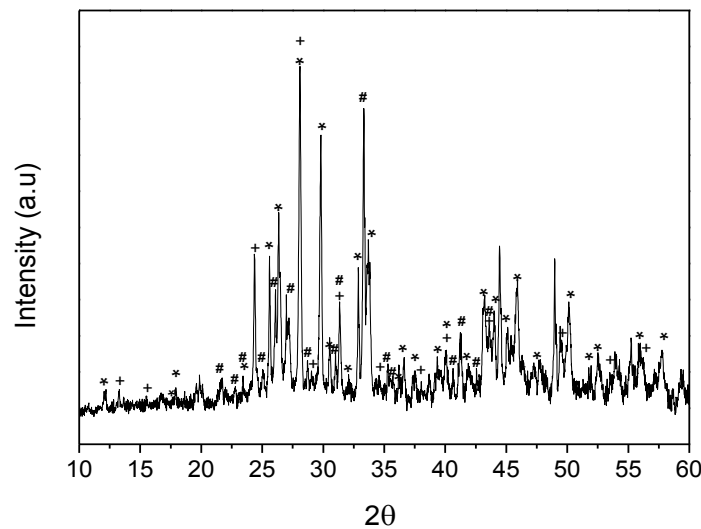
Figure 28. *XRD pattern of the target melted at 9 mA current (*Sr$_3$P$_4$O$_{13}$, $^+$Sr(PO$_3$)$_2$ and $^\#$NaSrPO$_4$)*

The XRD patterns exhibit sharp peaks indicating that independently of the current, the targets crystallize during the deposition. The peaks in the diffractogram were identified as the peaks of Sr$_3$P$_4$O$_{13}$ [04-015-2023], Sr(PO$_3$)$_2$ [00-044-0323] and NaSrPO$_4$ [00-033-1282]. Similar crystals were found to precipitate in the glass within similar glass system when heat treated at (T$_g$ + 20)°C for 17 hours and (T$_p$ − 40)°C for 12 hours in [Lo 2017].

4.2.1 Composition analysis of the thin films and of the targets

The composition of as deposited films and of the target was checked using Zeiss Cross-beam 540 Scanning Electron Microscope (SEM) with Oxford X-Max^N 80 EDS detector (see **Table 6** below). Note that the composition of the film was found to be independent of the substrate.

Table 6. Compositional analysis of the remaining glass targets and films

		P_2O_5 ±1.5 mol%	Na_2O ±1.5 mol%	SrO ±1.5 mol%	Er_2O_3 ±1.5 mol%	Yb_2O_3 ±1.5 mol%
REF Glass		46.2	9.1	42.3	0.6	1.9
5 mA	Target	50.4	19.3	28.9	0.3	1.1
		50.1	7.0	41.8	0.3	0.9
		46.3	8.0	43.9	0.5	1.4
	Film on Silicon	66.5	33.5	0.0	0.0	0.0
		66.5	33.5	0.0	0.0	0.0
9 mA	Target	45.8	8.4	42.7	0.8	2.4
		52.2	16.0	30.2	0.4	1.2
		38.6	6.9	52.5	0.5	1.6
	Film on Silicon	74.7	25.3	0.0	0.0	0.0
		74.0	26.0	0.0	0.0	0.0
13 mA	Target	37.3	5.3	54.0	0.9	2.5
		41.1	58.0	0.8	0.0	0.1
		40.2	9.8	44.6	1.4	4.0
	Film on Silicon	76.3	21.0	2.8	0.0	0.0
		77.1	20.2	2.7	0.0	0.0
		73.1	23.6	3.2	0.0	0.0
21 mA	target	48.9	0.9	45.6	1.1	3.5
		40.9	0.5	53.1	1.3	4.2
		52.9	11.9	33.8	0.3	1.1
	Film on Silicon	75.5	20.0	4.5	0.0	0.0
		72.4	23.7	3.8	0.0	0.0
		68.4	28.1	3.5	0.0	0.0

Sr and rare-earth free thin films were actually deposited independently of the deposition current. Based on the composition analysis of the thin films and of the remaining target, it is clear that there is uneven melting and evaporation of the elements from the glass during the film deposition; heavier elements such as Yb and Er remain in the target whereas the lighter elements such as P and Na evaporate. With an incease in the deposition current from 5 to 21 mA, the composition of the thin film (in mol%) changes from ($66P_2O_5$-$34Na_2O$) to ($77P_2O_5$-$18Na_2O$-$5SrO$) indicating that less Na and more Sr are deposited when depositing the film using higher current. Additional deposition trials should be performed using higher current in order to check if it is possible to deposit this phosphate film with the composition of the target.

4.2.2 Effect of substrate on the thin film surface quality

Figure 29 shows the images of thin films deposited on silicon and quartz substrates right after the deposition.

(a) On silicon substrate

(b) On quartz substrate
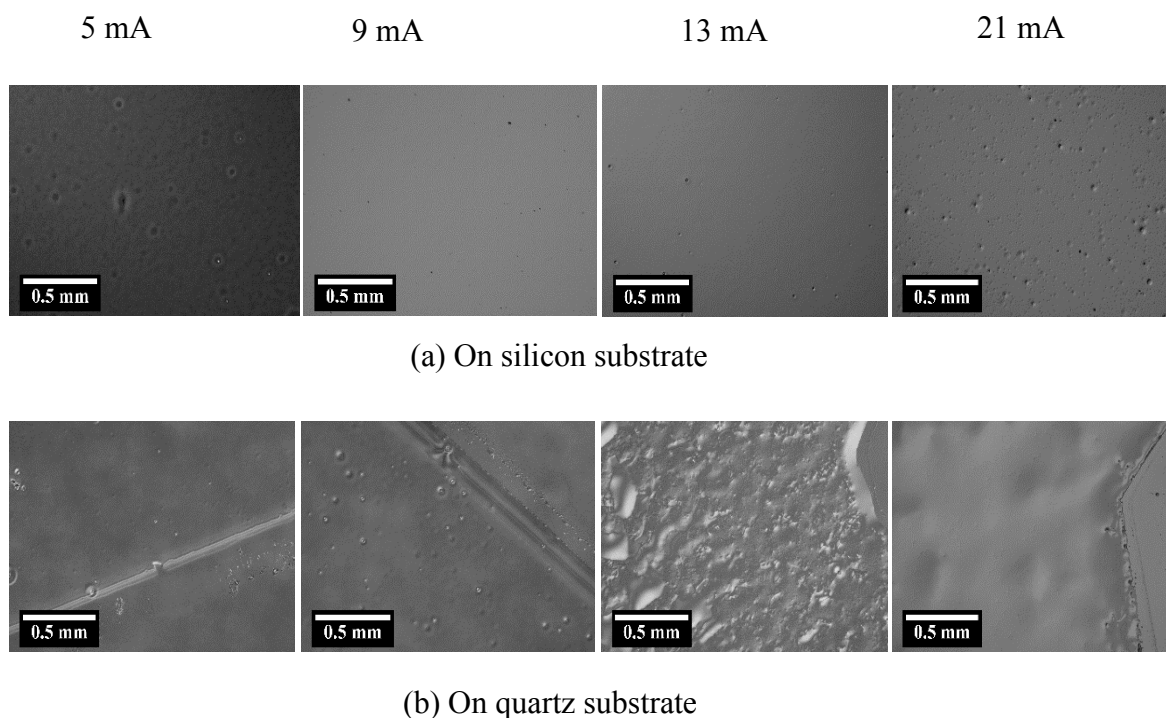
Figure 29. *Optical images of the thin-films deposited on silicon (a) and quartz (b) substrates using different deposition current*

It is clearly shown that the substrate has a significant impact on the surface quality of the thin films, independently of the current. The film seems to be deposited more uniformly on a silicon substrate than on the quartz slide. This is probably due to the different thermal expansion coefficient: the coefficient of thermal expansion (CTE) of soda phosphate glass ($50P_2O_5$-$50Na_2O$) was reported $2\times10^{-6}\,K^{-1}$ (in the temperature range 550-

700°C) [Dr 1985] while the expansion coefficient of silicon and quartz are $2.56\times10^{-6}\,\text{K}^{-1}$ and $0.59\times10^{-6}\,\text{K}^{-1}$, respectively.

In addition, we also noticed that the films were not stable overnight in nitrogen as illustrated in the **Figure 30** below.

(a)   (b)

As deposited films

Films after one night in nitrogen
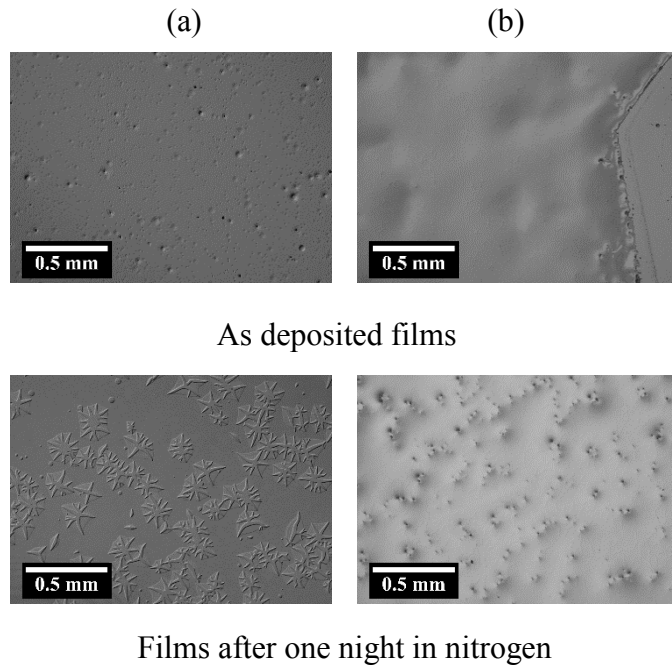
Figure 30. *Optical images of the thin films of as deposited and aged films deposited using 21 mA on silicon (a) and quartz (b)*

After one night in nitrogen, a large number of holes could be seen in the films deposited on quartz. The films also suffered delamination. Moreover, we noticed that after one night in nitrogen, the surface of the films deposited on silicon was different: defects can be seen. They look like crystals. However, if these defects are indeed crystals, the crystals formation during overnight stay at room temperature is not understood, as the precipitation of crystals requires high temperature.

As explained in [Oz 2006], mechanical properties of thin films such as adhesion, stability towards delamination etc. are mainly due to the residual stress that exist in the film regardless of the deposition techniques. Residual stresses might occur due to mismatch of the coefficient of thermal expanxion (CTE) of film and substrate, atom incorporation into growing film during deposition, lattice misfit with substrate, recrystallization processes, microscopic voids etc. Residual stresses in film are dynamic, they change over time, and if the energy release rate will exceed the fracture toughness of the film, it makes the film vulnerable to channel cracking. Crack propagation finally leads to peeling of the layer from the substrate.

Figure 31 shows the SEM images of the thin films after aging for a week in nitrogen environment.

5 mA   9 mA   13 mA   21 mA

(a) On silicon substrate
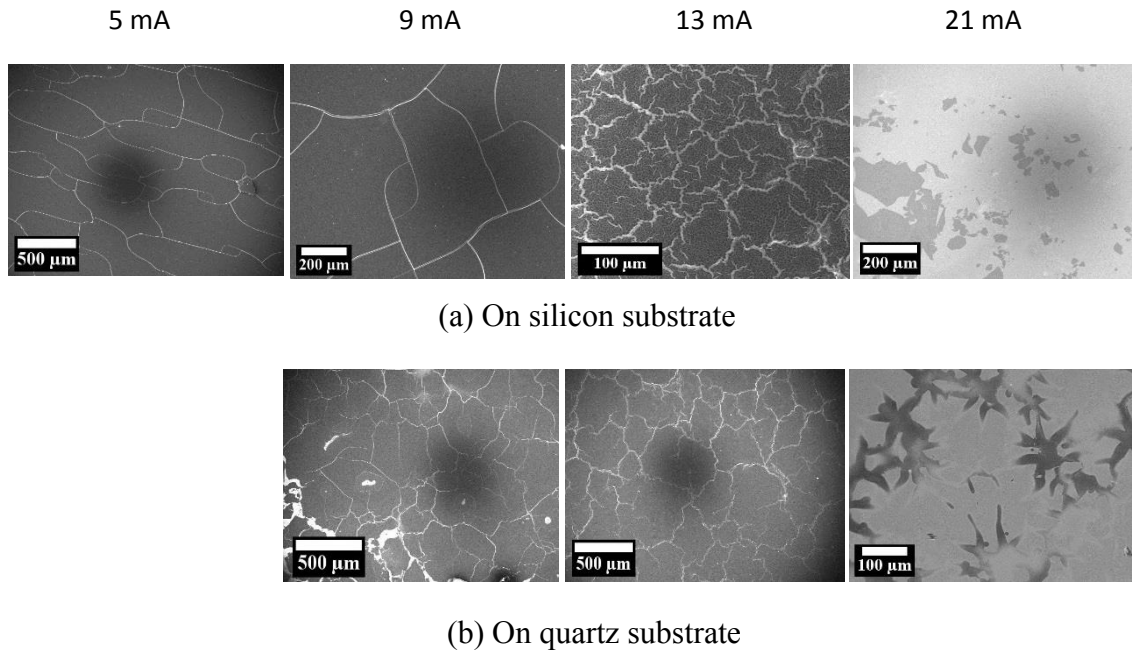

(b) On quartz substrate

Figure 31. *SEM pictures of the thin films deposited on silicon (a) and quartz (b) substrates after a week in nitrogen environment*

Upon a prolonged aging, local loss of adhesion was observed in the films because of stress release mechanism. For the films deposited using 5 and 9 mA, formation of elongated crack-like defects was seen under SEM while for the film deposited using 13 mA delamination mode involves wrinkling of film. These surface defects start from pre-existing blisters because of boundary instability triggered by the sample and the usual mode of their growth is by delamination of the tip. According to Stanko [Br 2017], aging in room temperature can create nano-voids by decomposition or reaction of film components which can further form additional pathways for gases like hydrogen and oxygen and form water. In our case, since phosphate glass have abundent OH$^-$ groups and since the deposition was made under elevated temperature, lots of such voids are expected to form during the deposition which later contribute to the unstability of the films under aging. According to [Ts 2005], it is also possible to relate cracking to subcritical or environmentally aided fractures, which are chemical reaction between some species in the environment and strained bonds.

4.2.3 Effect of annealing on the thin film delamination

Because the thin films are not stable overtime, an annealing of the thin film after deposition was tested in order to stabilize the thin films overtime. The thin films were annealed at 225°C for 5 hours in air. The films were placed in the furnace at high temperature. Note

that 225°C was chosen based on the glass composition of the thin film (high P_2O_5 mol%, see **Table 6**).

Figure 32 shows optical images of thin films taken after annealing at 225°C for 5 hours.

| 5 mA | 9 mA | 13 mA | 21 mA |

(a) On silicon substrate
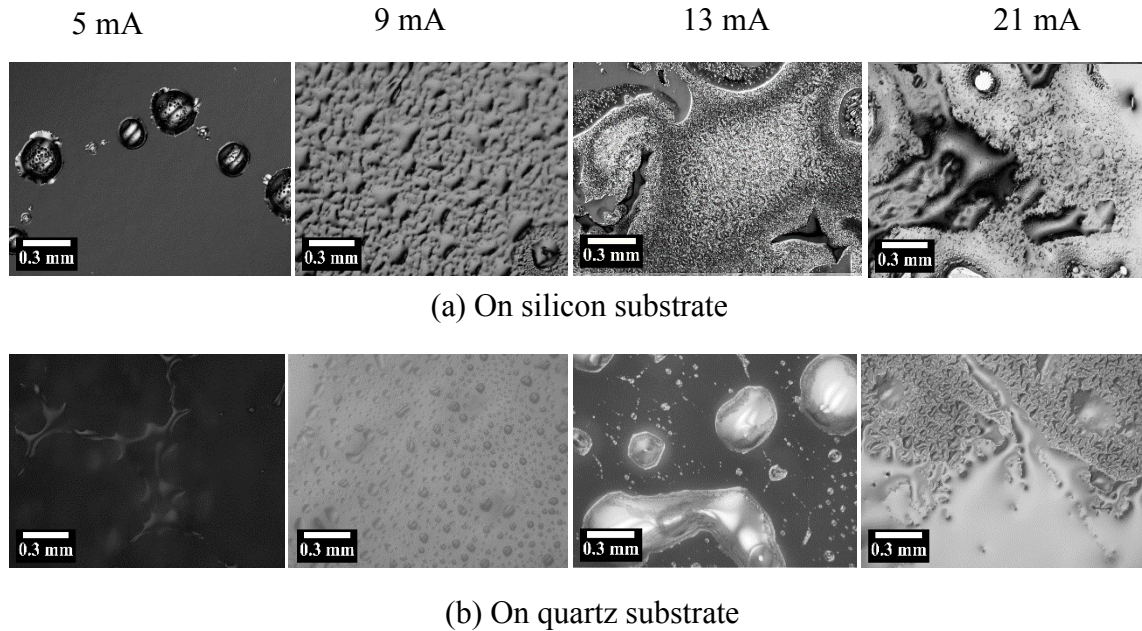

(b) On quartz substrate

Figure 32.   *Optical images of the thin films deposited on silicon (a) and quartz (b) substrates after annealing at 225°C for 5 hours.*

After annealing, the surface quality of the films was found to degrade; this could be the effect of thermal shock as the films were annealed at 225°C directly from the room temperature. In addition, mismatch of CTE of the film and substrate also might cause the film to lose its adhesion with the substrate as discussed in the previous paragraph. The films are subjected to compression during cooling which will cause spallation and delamination of the film as in [Ha 1997]. Additional trials should be performed in order to check if an annealing of the films using a slow heating rate could improve the stability overtime of the films.

4.3   Fiber waveguide: Fiber drawing and characterization

Unclad monoindex fiber were drawn from 10 cm long unstructured preforms with a 1 cm diameter prepared using the melting process. A 25 gram batch was melted for 45 min at 1150°C and then casted in a graphite mold, pre-heated at 300°C. After quenching, the preforms were annealed at 400°C for 10 hours. The bubble free preforms were sent to Rennes University (France) for drawing. The drawing process and drawing parameters can be found in the sections 2.5.2 and 3.1.3 respectively.

4.3.1 Thermal and structural properties of the fiber

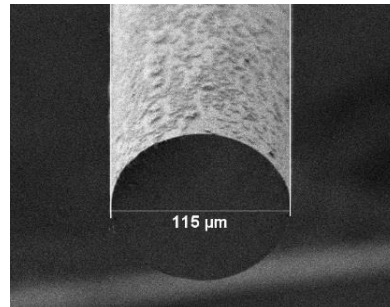A SEM picture of the fiber in **Figure 33** shows circular and concentric core.

Figure 33. *Cross sectional SEM image of fiber*

The fiber has a (115±1) µm diameter as planned. It is well known that the severe quenching under the imposed drawing stress can lead to detectable structural variation [Ma 2010]. Therefore, the thermal and structural properties of the fibers were measured and compared to those of the bulk. As shown in the **Table 7** below, slight decrease in T_g was observed after fiber drawing.

Table 7.   Comparison of thermal properties of the preform and the fiber

Sample code	T_g (°C) ±3	T_x (°C) ±3	T_p (°C) ±3	ΔT (T_x-T_g) (°C)
REF	462	580	593	118
Fiber	456	578	594	122

The IR absorption spectra of the preform and of the fibers are shown in the **Figure 34** below.
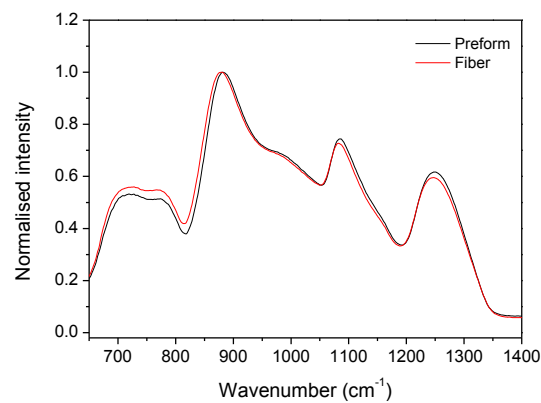

Figure 34.   *IR absorption spectra of the preform before and after drawing fiber*

The IR spectra of fiber exhibit similar bands and shoulder as that of preform. The variation in intensity and shift of the IR bands after drawing indicates that minor change in the structure of the glass occurs during the fiber drawing. The decrease in intensity of the shoulder at 980 cm^{-1} and of the band at 1085 cm^{-1} and small shift of band positions towards lower wavenumber after fiber drawing denotes that the fiber has weaker network connectivity and probably re-orientation of P-O-P bonds compared to that of bulk glass in agreement with decrease in T_g after fiber drawing. This change in glass structure might be due to severe quenching under the imposed drawing stress as discussed in [Ma 2010].

4.3.2 Optical properties of the fiber

The absorption spectra of the fiber for different lengths were measured using the optical spectrum analyzer (Ando, AQ-6315A) and stabilized broadband white light (Thorlabs SLS201L) as excitation source. The wavelength was measured with an accuracy of ± 1 nm. **Figure 35** shows the absorption spectrum for 1 cm fiber in visible and NIR region. It is composed of several bands corresponding to energy transition of Er^{3+} and Yb^{3+} ions.
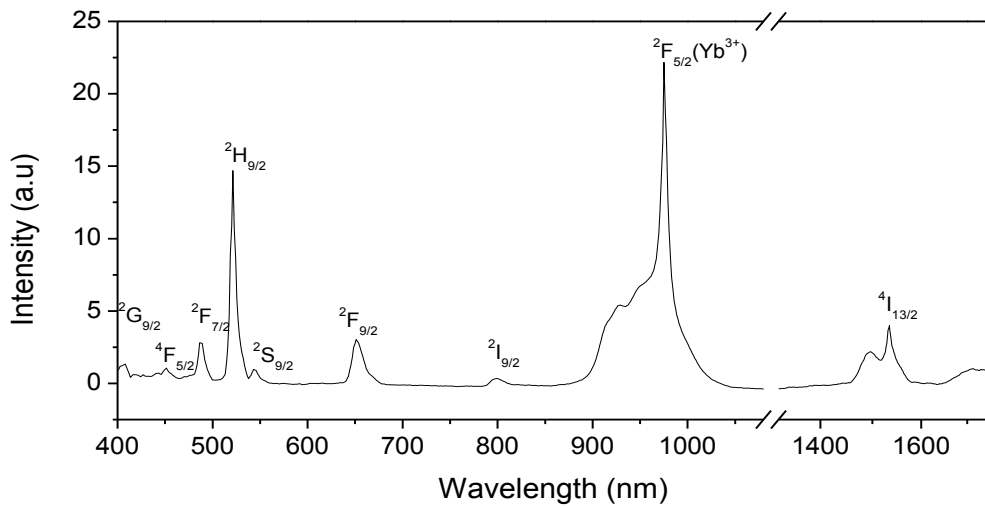
Figure 35.   *Absorption spectrum for 1 cm long fiber in visible and NIR region. All the absorption bands except at 975 nm are due to Er^{3+} ions.*

As explained in the section 4.1, all the absorption bands are due to transition from the ground state to the excited levels of Er^{3+} and Yb^{3+} ions as denoted in the figure. Losses were calculated assuming the losses only due to NA (Numerical Aperture) mismatch and the internal losses in fiber. NA of fiber under study was calculated to be 1.21 taking air as a clad. NA mismatch occurs due the difference in numerical aperture of transmitting half and receiving half of the fibers due to which all the light from the transmitting fiber cannot be coupled to the receiver end. Losses were calculated by cutback method and it ranged from 0.1 to 0.4 dB·cm^{-1} at 700 nm.

Figure 36 presents the comparison of absorption spectra of preform and the fiber.
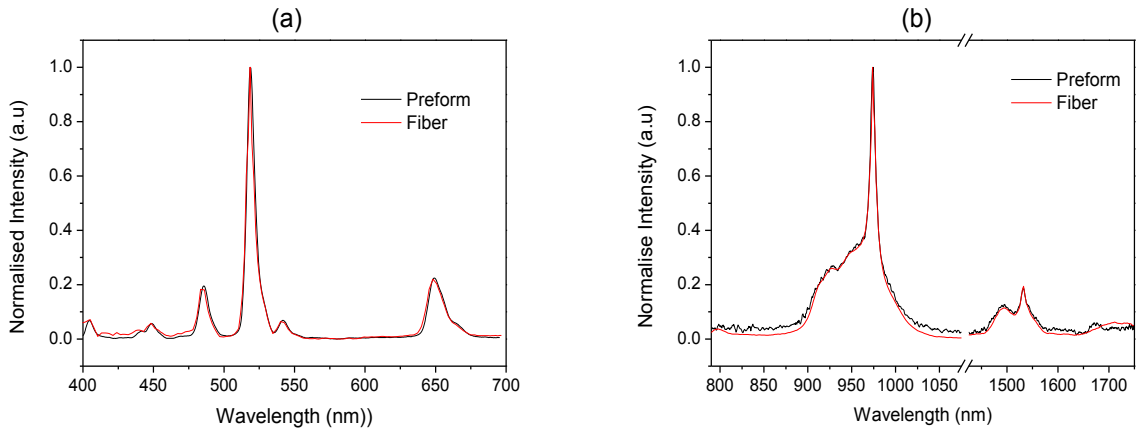

Figure 36. *Normalized absorption spectra of preform and fiber in Visible (a) and NIR (b) region*

It is evident from the **Figure 36** that the absorption spectra for both the preform and fiber are similar. Similar spectrum in NIR region is a proof that the RE sites have not changed during transformation of glass to fiber.

4.3.3 Emission properties of the fiber

The emission of fiber at NIR was investigated by pumping it with a laser diode of 975 nm. Observed emission spectra of 1 cm long fiber along with absorption spectra is shown in **Figure 37**. Short piece of fiber is not enough to absorb pump source fully, thus, emission spectrum denotes residual pump at 975 nm.
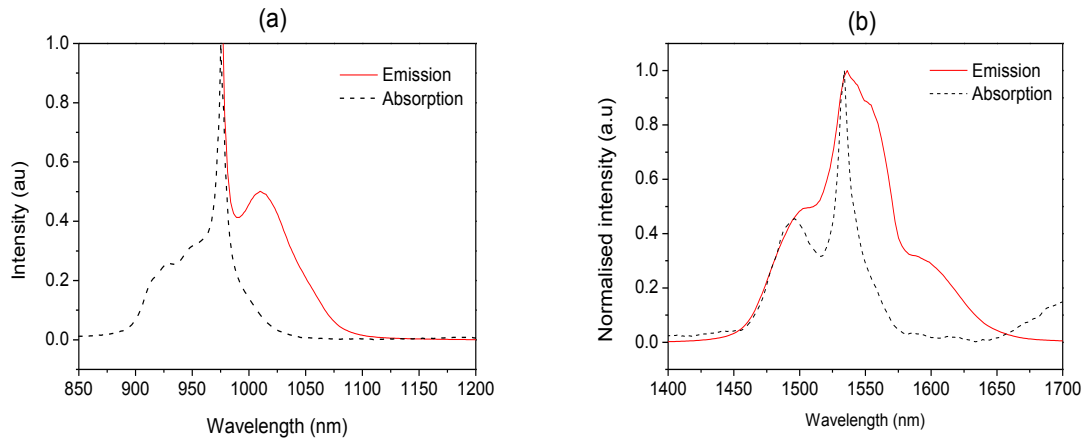
Figure 37. *Normalized emission (λ_{ex} = 975 nm) and absorption bands of investigated fiber centered at ~980 nm (a) and at ~1.5 µm (b)*

Two emissions wavelength ranges were detected for the fiber: one at 1.01 µm (**Figure 37a**) and the other at 1.5 µm (**Figure 37b**) clearly showing that Yb^{3+} ions acted both as an activator (emitter) and as a sensitizer. The presence of emission at 1.01 µm ($Yb^{3+}:{}^2F_{5/2}\rightarrow{}^2F_{7/2}$) is a result of quick saturation effect in energy transfer from Yb^{3+} to

Er^{3+} ions. The luminescence for Er^{3+} ions from the transition $^4I_{13/2} \rightarrow ^4I_{15/2}$ results in a broad band around 1.5 μm. The emission band at 1.5 μm measures 58 nm in bandwidth value, which is broader than that reported in [Su 2015]. Moreover, Bandwidth value approached 70 nm for 7 cm long fiber. Broadband emission is due to the inhomogeneous line broadening which originates due to the local site-to-site variation in emitting centers' surrounding [Be 1999].

Figure 38 shows the comparison of emission spectra of the fiber at 1.5 μm with that of bulk glass when pumped with 125 mW 975 nm laser.
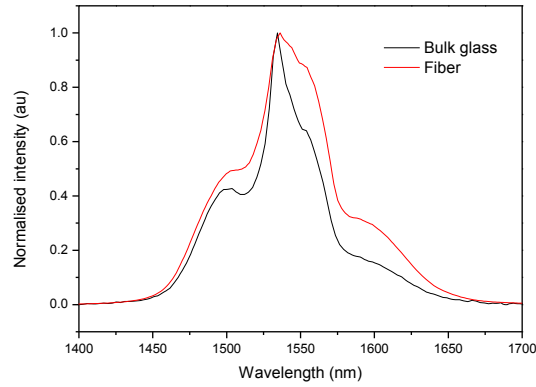
Figure 38.   *Emission spectra of bulk glass and fiber at λ_{ex} = 975 nm*

Broader emission spectrum was seen for fiber, probably due to the confinement of light in small dimension and due to the directional emission.

Figure 39 shows normalized emission for 1 cm long fiber at NIR when pumped with 975 nm excitation source and different pump powers. The spectrum intensity at 1.01 μm increased successively with increased pump power with respect to the emission at 1.5 μm.
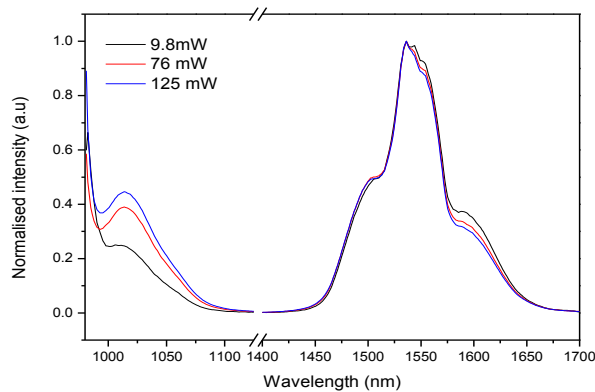
Figure 39.   *Normalized emission spectra for 1 cm long fiber at different pump power (λ_{ex} = 975 nm)*

The fiber also performs an increase of emission intensity at 1.5 μm due to the fact that Yb^{3+} ions acted as an activator rather than sensitizer. The sensitizer effect of Yb^{3+} is seen because lifetime of excited Yb^{3+} ions should be shorter than the rate of energy transfer and the lifetime of Er^{3+} in the fiber within P_2O_5-SrO-Na_2O compositional space.

Figure 40 shows the emission spectra for different lengths of fiber. For longer pieces of fiber, the emission spectrum is not uniform anymore and the emission spectra at 1.01 μm and 1.5 μm shifts towards longer wavelength when fiber are pumped with 125 mW laser diode. Additionally, pronounced peaks and dips are observed in emission bands at 1.5 μm number of which increases with increased length of fiber.
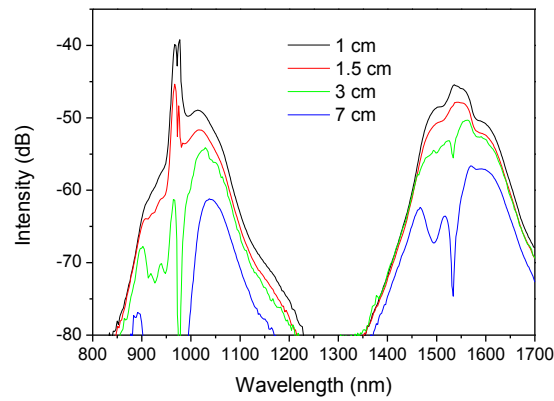
Figure 40.   *Emission spectra for different lengths of fiber at $\lambda_{ex} = 975$ nm*

As reported in [Na 2008] this is a distinct sign of spectral hole-burning effect. This is due to strong reabsorption at particular spectral wavelength of Yb^{3+} and Er^{3+} ions. Strong absorption must have occurred due to the higher concentration of RE ions (shown in **Table 3**) and insufficient pump power to stimulate the emission. The decrease in intensity of emission can be related to the fiber imperfection and its monoindex profile, which allow light leakage through its air-glass interface [Sh 1998]. Spectral hole-burning effect is also consequence of inhomogeneous line broadening which is caused due to amorphous nature of glass, random distribution of dopants and host imperfection [Mo 1988].

5. CONCLUSIONS

In this thesis, glasses with the system $(98-x-y)(0.50P_2O_5-0.40SrO-0.10Na_2O)-0.5Er_2O_3-1.5Yb_2O_3-xZnO-yY_2O_3$ (in mol%) were prepared using melt-quenching technique. The physical, thermal, structural, optical and spectroscopic properties of the glasses were measured. The density increased with an increase in x and y. Thermal stability factor, ΔT, of the investigated glasses was well above 100°C indicating that these phosphate glasses are thermally stable and good candidates for film deposition and fiber drawing. From the IR and Raman spectra, the structure of the glass is suspected to be a metaphosphate structure with Q^2 and Q^1 network units. We expect ZnO to act as a network modifier, in agreement with the decrease in T_g which can be explained as depolymerization of phosphate network. Y_2O_3 is thought to lead to the formation of P−O−Y at the expense of P−O−P bonds increasing the T_g. While ZnO and Y_2O_3 have an impact on the structure of the glass, they have no significant impact on the sites of the Er^{3+} and Yb^{3+} ions. Er^{3+} and Yb^{3+} ions are thought to be surrounded mainly by P, Na and Sr. Under excitation at 975 nm, the glasses exhibit a broad emission at 1.5 µm due to $^4I_{13/2} \rightarrow {}^4I_{15/2}$ ion transition in Er^{3+}.

Glasses with $y = 1.25$ and 2.5 were prepared with larger Er_2O_3 and Yb_2O_3 to improve the spectroscopic properties of the glasses. Although these glasses have a stronger emission at 1.5 µm when using 975 nm excitation compared to the other glasses, their melting temperature and melt viscosity are too high to allow us to prepare target for film deposition and preform for fiber drawing with good quality. Therefore, the glass with the composition $49P_2O_5-39.2SrO-9.8Na_2O-0.5Er_2O_3-1.5Y_2O_3$ (in mol%) was selected for film deposition and fiber drawing.

Phosphate glass thin films were deposited using e-beam evaporation. The pressure of vaccum chamber was 4.8 to 4.0×10^{-5} Torr. The glass was deposited on silicon and quartz substrates using electron beam of 9 kV and current ranging from 5 to 21 mA. Composition analysis of the films using SEM coupled with an EDS showed that as deposited films contain no heavier RE elements. Additionally, the stability of the phosphate glass films was also an issue. Spallation and delamination were seen for the samples aged for a weak in nitrogen environment, which was related to release of residual stress building up during or after deposition. Post deposition annealing was tested to increase the film stability but was unsuccessful. With this study, we clearly showed that complex composition of the target means adjusting different parameters like pressure of the deposition chamber, working distance, acceleration voltage, deposition current, temperature to be able to deposit films with the composition of the target. The background pressure of the chamber must be low enough to yield a mean-free path for all the constituents molecules which is much shorter than source-substrate distance. Further research on optimizing the

parameters and also the annealing process has to be performed to deposit Er^{3+}, Yb^{3+} codoped phoshate glass into thin films. Special target preparation technique such as compaction of glass crunched into powder for example can also be tested to get uniform evaporation. Finally, it is crucial to understand the mechanism of stress formation during the film deposition in order to control the residual stresses in thin films. However, methods to reduce internal stresses may include lowering the deposition rate, changing the substrate material or modifying its surface with other elements, selecting optimal temperature for deposition.

Core-only fiber with average diameter of 115 μm was successfully drawn by the team in the Glass and Ceramic group at Rennes University in France from preform (10 cm in length and 1 cm in diameter). Fiber retained its metaphosphate structure, as checked using IR spectroscopy. Losses were measured by cutback method and were found to be 0.1-0.4 dB·cm^{-1} at 700 nm. Emission was collected at NIR from fibers with different length. Broad emission spectra was observed at 1.5 μm, the bandwidth of which approached to 70 nm, which is broader than that for Er^{3+} doped silica glass fiber. Aditionally, emission band at ~1 μm was seen as Yb^{3+} acted as an activator which saturated the emission at 1.5 μm which can be eleminated by using moderate pump power or increasing the ratio of Er/Yb in the glass network.

Broadband emission at 1.5 μm in phosphate glass makes it a possible candidate for various biomedical applications as 1.5 μm laser wavelength is eye safe. Similarly, it can be used in LIDAR (Light Detection and Ranging) and for military applications, as it is invisible to night vision cameras. On the other hand, spectral hole-burning effect has potential for technological application to optical data storage and optical signal processing, laser frequency stabilization, portable frequency standard, etc.

As for future work on fiber drawing, raw materials with higher purity could be used as well as purification and dehydration of the glass batch prior to the melting could be tested to further reduce the fiber losses. Core-clad fiber could be drawn from core-clad preform prepared using a rotational caster avalaible at TUT.

References

[Ad 1976] Addiss, R. R. and Albertinetti, N. P."Process for coating glass onto polymeric substrates" U.S Patent 3,953,652, issued April 27, 1976.

[Ad 2016] *AD-net.* 04 21, 2016. http://www.ad-net.com.tw/structure-of-fiber-optics-cable/ (accessed 04 30, 2017).

[Ag 2001] Agrawal, G. P. *Nonlinear Fiber Optics.* Third Edition. San diego, California : Academic Press, 2001, 467 pages.

[Ba 1994] Barrière, A. S, Raoux, S., Garcia, A., L'Haridon, H., Lambert, B., and Moutonnet, D. "Intra4fshell transitions at room temperature of Er^{3+} ions in Ca_{1-x} Er_x F_{2+x} thin films grown on Si(100)." *Journal of Applied Physics*, 75 (1994): 1133-1137.

[Ba 2001] Ball, D.W. "Theory of Raman Spectroscopy." *Spectroscopy* 16, (2001): 32-34.

[Be 1999] Becker, P. M., Olsson, A. A and Simpson, J. R. *Erbium-doped fiber Amplifiers: Fundamentals and Technology.* Academic Press, 1999, 460 pages.

[Bh 2002] Bhadeshia, H. K. D. H. "Differential Scanning Calorimetry." University of Cambridge, 2002.
Available online: https://www.phase-trans.msm.cam.ac.uk/2002/Thermal2.pdf

[Br 1997] Brow, R.K, and David, R.T. "Structural design of sealing glasses." *Journal of Non-Crystalline Solids* 222, (1997): 396-406.

[Br 2009] Brow, R. K, and Melodie, L. "A survey of energy and environmental applications of glass." *Journal of the European Ceramic Society*, 29, (2009): 1193-1201.

[Br 2000] Brow, R. K " Review: the structure of simple phosphate glasses." *Journal of Non-Crystalline Solids* 263 & 264 (2000): 1-28.

[Br 2017] Brankovic, S. R. "Crack Formation during Electro deposition and Post-deposition Aging of Thin Film Coatings." *NASF Surface Technology White Papers* 81, (2017): 13-19.

[Ch 1994] Chi, C. "An e-beam evaporated borosilicate glass thin film as an encapsulant for annealing Be-implant InP." *Materials chemistry and Physics* 39 (1994): 69-71.

[Dr 1985] Drotning, W. D. "Thermal expansion of glasses in the solid and liquid phases." *International Journal of Thermophysics* 6, (1985): 705-714.

[Fa 2003] Faupel, F., Frank, W., Macht, M. P., Mehrer, H., Naundorf, V., Rätzke, K., Schober, H. R., Sharma, S. K., Teichler, H. "Diffusion in Metallic Glasses and Supercooled melts." *Reviews of Modern Physics* 75, (2003): 237-280.

[Fr 2000] Franz, J. H., and. Jain, V. K. *Optical Communications: Components and Systems.* New Delhi: Narosa Publishing House, 2000, 717 pages.

[Ga 2006] Gan, F., and Xu, L. *Photonic Glasses.* World Scientific Pubishing Co. Pte. Ltd, 2006, 447 pages.

[Gh 1998] Ghatak, A. , and Thyagarajan. K. *Introduction to Fiber Optics.* Cambridge: Cambridge University Press, 1998, 565 pages.

[Go 2005]:Goel, N. K. "Development of core suction technique for fabrication of highly doped fibers for optical amplification and characterization of optical fibers for Raman amplification", *PhD dissertation*, Virginia polytechnic Institute (2005).

[Go 2006] Goel, N. K., Stolen, R. H., Morgan, S., Kim, J. K., Kominsky, D. and Pickrell G. "Core-suction technique for the fabrication of optical fiber preforms." *Optic Letters* 31, (2006): 438-440.

[Go 2007] Goldstein, J., Newbury, D.E., Joy, D.C., Lyman, C.E., Echlin, P., Lifshin, E., Sawyer, L., Michael, J.R *Scanning Electron Microscopy and X-Ray Microanalysis.* United State of America: Springer, 2007, 689 pages.

[Ha 1997] Haanappel, V.A.C, VandenBerg, A. H. J., VanCorbach, H. D., Fransen, T. and Gellinhs, P.J . "The effect of thermal annealing on aherence of Al_2O_3 films deposited by LP-MOCVD on several high alloy steels." *Journal of Adhesion Science and Technology* 11, (1997): 905-919.

[Ha 2001] Hamdi, M, and Ektessabi, A. M. "Electron beam deoposition of thin bioceramic film for biomedical implants." *Thin Solid Films* 398-399, (2001): 358-390.

[Heraeus] *Thermal Properties of Fused Silica.*
Avaiable online www.heraeus-quarzglas.com (accessed 3 May, 2017).

[He 1954] Heel, A. C. S. V. "A new method of transporting optical images without aberrations." *Nature* 173, (1954):39.

[He 2009] He, B. *Two-Dimensional X-Ray Diffraction.* Wiley, 2009, 426 pages.

[Ho 2004] Hollas, M. J. *Modern Spectroscopy.* Fourth Edotion. John Wiley and Sons, Ltd, 2004, 482 pages.

[Hu 2014] Husband, T. "The sweet science of candy making." chemmatters, 2014.

[Hu 2016] Hughes, M. *The Global source SEMICORE.* 15 June, 2016. Available online http://www.semicore.com/news/89-what-is-e-beam-evaporation (accessed 29 June, 2017).

[Ka 2001] Karabulut, M, Melnik, E., Stefan, R., Marasinghe, G. K., Ray, C. S., Kurkjian, C. R. and Day, D. E. "Mechanical and Structural properties of phosphate glasses." *Journal of Non-Crystalline Solids* 288, (2001): 8-17.

[Ko 2010] Konidakis, I., Varsamis, C. P. E., Kamitsos, E. I.,Moncke, D., and Ehrt, D. "Structure and Properties of Mixed Strontium-Manganese Metaphosphate Glasses." *Journal of Physical Chemistry C*, (2010): 9125-9138.

[Kr 1979] Kravchenko, V. B., and Rudnitsku, Yu. P. "Phosphate laser glasses." *Soviet Journal of Quantum Electronic* 9, (1979): 399-415.

[Kr 2016] Karmakar, B., Rademann, K., and Stepanov, A. *Glass-nanocomposites: Synthesis, Properties and Applications.* Elsevier S&T Frontlist Promotion 2016, 408 pages.

[Le 2007] Lee, E.T.Y., Taylor, E.R.M. "Two-die assembly for the extrusion of glasses with dissimilar thermal properties for fibre optic preforms", *Journal of Materials Processing Technology* 184, (2007) 325-329.

[Li 1997] Liu , H.S; Chin, T.S; Yung, S.W. "FTIR and XPS studies of low melting PbO-ZnO-P2O5 glasses." *Materials Chemistry and Physics* 50, (1997): 1-10.

[Li 2003] Lifante, G. *Intregated Photonics: Fundamentals.* John Wiley & Sons Ltd, 2003, 198 pages.

[LibreTexts] LibreTexts. *How an FTIR Spectrometer Operates.* 02 17, 2017. https://chem.libretexts.org/Core/Physical_and_Theoretical_Chemistry/Spectrosc opy/Vibrational_Spectroscopy/Infrared_Spectroscopy/How_an_FTIR_Spectrom eter_Operates (accessed 05 09, 2017).

[Lo 2017] Lopez-Iscoa, P., Salminen, T., Hakkarainen, T., Petit, L., Janner, D., Boetti, N. G., Lastusaari, M., Pugliese, D., paturi, P. and Milanese, D. "Effect of partial crystallization on the spectroscopic properties of Er^{3+} doped phosphate glasses." *Materials* 10 (2017): 473.

[Ma 1980] MacChesney, J. B. "Materials and Processes for Preform Fabrication-Modified Chemical Vapor Deposition and Plasma Chemical Vapor Deposition" *Proceedings of IEEE* 68,(1980): 1181-1980.

[Ma 2009] Massera, J. "Nucleation and growth behaviour of tellurite-based glasses suitable for mid-infrared applications." *PhD dissertation*, Graduate school of Clemson University (2009).

[Ma 2010] Massera, J., Haldeman, A., Milanese, D., Gebavi, H., Ferraris, M., Foy, P., Hawkins, W., Ballato, J., Stolen, R., Petit, L. and Richardson, K. "Processing and characterization of core–clad tellurite glass preforms and fibers fabricated by rotational casting." *Optical Materials* 32, (2010): 582–588.

[Mi 2001] Miniscalco W.J. "Optical and Electronic Properties of Rare Earth Ions in Glass." In *Rare Earth Doped Fiber Laser and Amplifiers, Revised and Expanded*, edited by Michel J.F Digonnet, CRC Press, 2001, 798 pages

[Mo 1988] Moerner, W. E. *Persistant Spectral Hole-Burning: Science and Applications*, Springer-Verlag Berlin Heidelberg, 1988, 315 pages.

[Na 2008] Nandi, P., and Jose, G. "Superfluorescence from Yb- and Yb–Er-doped phosphotellurite glass fibres." *Optical Fiber Technology* 14, (2008): 275–280.

[Na 2015] Narayanan, M. K, and Shashikala H. D. "Statistical optimization of melt-quenching process parameters for multiple properties of ternary barium phosphate glasses." *Materials Chemistry and Physics* 152, (2015): 127-134.

[Oz 2006] Ozen, I, and Mahmet A. G. "Residual Stress Relaxation and Microstructure in ZnO Thin Films." *Advances in Science and Technology* 45, (2006): 1316-1321.

[Pa 2008] Paschotta, R. "Rare-Earth-doped fibers" in the *Encyclopedia of Laser Physics and Technology* first edition, Wiley-VCH, 2008, 856 pages.

[Ra 2012] Rasmussen, S. C. *How glass changed the world.* Springer, 2012, 85 pages.

[Ra 2013] Rao, B. L., Babu, Y. N. C. R and Prasad, S. V. G. V. A. "Spectroscopic and EPR studies on $PbO-Y_2O_3-P_2O_5$ glasses doped with molybdenum ion." *Physica B* 429, (2013): 68-72.

[Ri 2004] Righini, G. C., and Andrea, C. "Glass optical waveguides: a review of fabrication techniques." *Optical Engineering* 53, (2004): 071819: 1-14.

[Sc 2004] Schwarz, J., Ticha, H., Tichy, H. and Mertens, R. "Physical Properties PbO-$ZnO-P_2O_5$ glasses I. Infrared and Raman spectra." *Journal of Optoelectronics and Advanced Materials* 6, (2004): 737-746.

[Sc 2014] Schuster, K, Unger, S., Aichele, C., Lindner, F., Grimm, S., Litzkendorf, D., Kobelke, J., Bierlich, J., Wondraczek, K. and Bartelt, H. "Material and technology trends in fiber optics." *Advanced Optical Technology* 3, (2014): 447-468.

[Sh 1998] Shangguan, H. Q. and Casperson, L. W. "Estimation of scattered light on the surface of unclad optical fiber tips: a new approach." *Optics Communications* 152, (1998): 307–312.

[Si 2005] Singh, J. and Wolfe, D. E. "Nanostructured Component Fabrication by Electron Beam-Physical Vapor Deposition." *Journal of Materials Engineering and Performance* 14, (2005): 448-459.

[Sn 1965] Snitzer E, and Woodcock.R "Yb^{3+} - Er^{3+} Glass Laser." *Applied Physics Letter* 6, (1965): 45-46.

[Su 2015] Subramaniam, T. K. "Erbium Doped Fiber Lasers for Long Distance Communication Using Network of Fiber Optics." *American Journal of Optics and Photonics* 3, (2015): 34-37.

[Ts 2005] Tsui, T. Y., and Andrew, J. M. "Constraint effect on thin film channel cracking behaviour." *Journal of material research Society* 20, (2005): 2266-2273.

[Ya 2000] Yamane, M and Yoshiyuki, A. *Glasses for photonics.* Cambridge Univ. Press, 2000, 284 pages**.**

[Za 1932] Zachariasen, W. H. "The atomic arrangement in glass", *Journal of the American Chemical Society* 54, (1932): 3841-3851.